



LUND UNIVERSITY

Time-Resolved X-ray Diffraction Studies of Laser-Induced Dynamics in Solids

Bengtsson, Åsa

2022

Document Version:

Publisher's PDF, also known as Version of record

[Link to publication](#)

Citation for published version (APA):

Bengtsson, Å. (2022). *Time-Resolved X-ray Diffraction Studies of Laser-Induced Dynamics in Solids*. Division of Atomic Physics, Department of Physics, Faculty of Engineering, LTH, Lund University.

Total number of authors:

1

General rights

Unless other specific re-use rights are stated the following general rights apply:

Copyright and moral rights for the publications made accessible in the public portal are retained by the authors and/or other copyright owners and it is a condition of accessing publications that users recognise and abide by the legal requirements associated with these rights.

- Users may download and print one copy of any publication from the public portal for the purpose of private study or research.
- You may not further distribute the material or use it for any profit-making activity or commercial gain
- You may freely distribute the URL identifying the publication in the public portal

Read more about Creative commons licenses: <https://creativecommons.org/licenses/>

Take down policy

If you believe that this document breaches copyright please contact us providing details, and we will remove access to the work immediately and investigate your claim.

LUND UNIVERSITY

PO Box 117
221 00 Lund
+46 46-222 00 00

Time-Resolved X-ray Diffraction Studies of Laser-Induced Dynamics in Solids

ÅSA BENGTTSSON

FACULTY OF ENGINEERING | LUND UNIVERSITY



Time-Resolved X-ray Diffraction Studies of Laser-Induced
Dynamics in Solids

Time-Resolved X-ray Diffraction Studies of Laser-Induced Dynamics in Solids

Åsa Bengtsson




LUND
UNIVERSITY

Thesis for the degree of Doctor of Philosophy
Thesis advisor: Prof. Jörgen Larsson. Co-advisor: Dr Henrik Enquist
Faculty opponent: Prof. Matias Bargheer

To be presented, with the permission of the Faculty of Engineering of Lund University, for
public criticism in the Rydberg Lecture Hall at the Division of Atomic Physics
Department of Physics on Friday, the 18th of March 2022 at 9:15.

Organization LUND UNIVERSITY Division of Atomic Physics Department of Physics P.O. Box 118 SE-221 00 LUND, Sweden		Document name DOCTORAL DISSERTATION	
		Date of disputation 2022-03-18	
		Sponsoring organization	
Author Åsa Bengtsson			
Title and subtitle Time-Resolved X-ray Diffraction Studies of Laser-Induced Dynamics in Solids			
Abstract <p>X-ray diffraction is an invaluable tool in the field of structural dynamics. In the work described in this thesis, time-resolved X-ray diffraction experiments were carried out to investigate ultrafast lattice dynamics. Ultrashort laser pulses were used to induce non-thermal melting and large-amplitude strain waves, and X-rays were used to probe these phenomena.</p> <p>Non-thermal melting was studied in indium antimonide (InSb). It was found that the inertial model, which states that the motion of the atoms is determined by their initial vibrational energy at the time of laser irradiation, accurately describes the process of non-thermal melting. It was demonstrated that the model is valid over a large range of temperatures, from 35 to 500 K, when taking the zero-point energy into account at low temperatures. It was also shown how the process of non-thermal melting can be used as a timing monitor to determine the relative timing of laser and X-ray beams in pump/probe experiments.</p> <p>It was shown how the use of an opto-acoustic transducer could reduce the duration of an X-ray pulse. The transducer was made of a thin gold film deposited on the surface of bulk InSb. Upon heating the thin gold film with an ultrashort laser pulse, a strain wave was generated in the semiconductor. This resulted in a modulated phonon spectrum and X-ray reflectivity. It was shown that a 100 ps long X-ray pulse can be transformed to a 20 ps pulse with an 8% efficiency.</p> <p>A large-amplitude strain wave was generated in graphite using an ultrashort laser pulse to elucidate the potential role of strain in phase transitions. The temporal evolution of the strain wave was mapped, and the pressure deduced. It was found that it was possible to induce a pressure and temperature corresponding to the region in the carbon phase diagram in which diamond can form.</p>			
Key words Time-resolved X-ray diffraction, Ultrafast, phonons, pressure wave, non-thermal melting			
Classification system and/or index terms (if any)			
Supplementary bibliographical information		Language English	
ISSN and key title 0281-2762, Lund Reports on Atomic Physics, LRAP 579		ISBN 978-91-8039-184-9 (print) 978-91-8039-183-2 (pdf)	
Recipient's notes		Number of pages 145	Price
		Security classification	

I, the undersigned, being the copyright owner of the abstract of the above-mentioned dissertation, hereby grant to all reference sources the permission to publish and disseminate the abstract of the above-mentioned dissertation.

Signature  _____

Date 2022-02-11

Time-Resolved X-ray Diffraction Studies of Laser-Induced Dynamics in Solids

Åsa Bengtsson



LUND
UNIVERSITY

pp i-70 © Åsa Bengtsson 2022

Paper I ©2017 AIP Publishing LLC

Paper II ©2018 International Union of Crystallography

Paper III ©2019 AIP Publishing LLC

Paper IV ©2020 American Physical Society

Paper V ©2020 AIP Publishing LLC

Paper VI ©by the authors (Manuscript unpublished)

Division of Atomic Physics
Department of Physics
Faculty of Engineering
Lund University
P.O Box 118
SE-221 00 Lund SWEDEN

ISBN: 978-91-8039-184-9 (print)

ISBN: 978-91-8039-183-2 (pdf)

ISSN: 0281-2762

Lund Reports on Atomic Physics, LRAP 579 (2022)

Printed in Sweden by Media-Tryck, Lund University, Lund 2022



Media-Tryck is a Nordic Swan Ecolabel certified provider of printed material. Read more about our environmental work at www.mediatryck.lu.se

MADE IN SWEDEN 

Dedicated to my family

Contents

Abstract	iii
List of publications	iv
Acknowledgements	vii
Popular Scientific Summary	ix
Populärvetenskaplig sammanfattning	xi
I Overview	1
1 Introduction	3
2 Matter and Light	5
2.1 Matter	5
2.2 Light	8
2.2.1 The pump laser	8
2.2.2 The X-ray probe	9
3 Light-Matter Interactions	11
3.1 Heating	11
3.2 Melting	13
3.3 Laser-induced periodic structures	14
3.4 Strain generation	15
3.5 Large-amplitude strain	17
3.6 Strain in a thin film	17
3.7 Modulating the phonon spectrum	18
4 Principles of X-ray Diffraction and Generation	21
4.1 X-ray scattering	21
4.1.1 Scattering by a single electron	21
4.1.2 Scattering by an atom	22
4.1.3 Scattering by a crystal: Bragg's law	23
4.1.4 Reciprocal space	23
4.1.5 The Ewald sphere	24
4.1.6 The structure factor	25
4.1.7 Imperfect and perfect crystals	26

4.2	X-ray generation	26
4.3	The FemtoMAX beamline	29
5	X-ray Diffraction Experiment Techniques	31
5.1	Symmetric and asymmetric crystals	31
5.2	Coplanar and non-coplanar geometry	32
5.3	Determining the angle of incidence	33
5.4	Probe depth	34
5.5	Space-time mapping for high temporal resolution	34
5.6	Measuring disorder	36
5.7	Measuring strain	37
6	Strain Generation and Melting	39
6.1	Large-amplitude strain wave in graphite	39
6.2	Non-thermal melting in InSb	43
6.3	Transition between thermal and non-thermal melting	47
7	Controlling and Diagnosing the Temporal Properties of X-rays	49
7.1	An X-ray switch based on a photo-acoustic transducer	49
7.2	Non-thermal melting of InSb as a timing monitor	51
8	Summary and Outlook	57
8.1	Summary	57
8.2	Outlook	58
	References	58
II	Papers	67
	Author's contributions	69

Abstract

X-ray diffraction is an invaluable tool in the field of structural dynamics. In the work described in this thesis, time-resolved X-ray diffraction experiments were carried out to investigate ultrafast lattice dynamics. Ultrashort laser pulses were used to induce non-thermal melting and large-amplitude strain waves, and X-rays were used to probe these phenomena.

Non-thermal melting was studied in indium antimonide (InSb). It was found that the inertial model, which states that the motion of the atoms is determined by their initial vibrational energy at the time of laser irradiation, accurately describes the process of non-thermal melting. It was demonstrated that the model is valid over a large range of temperatures, from 35 to 500 K, when taking the zero-point energy into account at low temperatures. It was also shown how the process of non-thermal melting can be used as a timing monitor to determine the relative timing of laser and X-ray beams in pump/probe experiments.

It was shown how the use of an opto-acoustic transducer could reduce the duration of an X-ray pulse. The transducer was made of a thin gold film deposited on the surface of bulk InSb. Upon heating the thin gold film with an ultrashort laser pulse, a strain wave was generated in the semiconductor. This resulted in a modulated phonon spectrum and X-ray reflectivity. It was shown that a 100 ps long X-ray pulse can be transformed to a 20 ps pulse with an 8% efficiency.

A large-amplitude strain wave was generated in graphite using an ultrashort laser pulse to elucidate the potential role of strain in phase transitions. The temporal evolution of the strain wave was mapped, and the pressure deduced. It was found that it was possible to induce a pressure and temperature corresponding to the region in the carbon phase diagram in which diamond can form.

List of publications

This thesis is based on the following publications, referred to by their Roman numerals:

- I **Communication: Demonstration of a 20 ps X-ray switch based on a photoacoustic transducer**
A. Jarnac, X. Wang, **Å. Bengtsson**, . C. Ekström, H. Enquist, A. Jurgilaitis, D. Kroon, A. I. H. Persson, V.-T. Pham, C. M. Tu, and J. Larsson.
Structural Dynamics 4, 051102 (2017)

- II **FemtoMAX - an X-ray beamline for structural dynamics at the short-pulse facility of MAX IV**
H. Enquist, A. Jurgilaitis, A. Jarnac, **Å. Bengtsson**, M. Burza, F. Curbis, C. Disch, J. C. Ekström, M. Harb, L. Isaksson, M. Kotur, D. Kroon, F. Lindau, E. Mansten, J. Nygaard, A. I. H. Persson, V. T. Pham, M. Rissi, S. Thorin, C.-M. Tu, E. Wallén, X. Wang, S. Werin and J. Larsson.
J. Synchrotron Rad. 25, 570-579 (2018)

- III **Generation of a large compressive strain wave in graphite by ultrashort-pulse laser irradiation**
Xiaocui Wang, A. Jarnac, J. C. Ekström, **Å. Bengtsson**, F. Dorchie, H. Enquist, A. Jurgilaitis, M. N. Pedersen, C.-M. Tu, M. Wulff, and J. Larsson.
Structural Dynamics 6, 024501 (2019)

- IV **Role of thermal equilibrium dynamics in atomic motion during nonthermal laser-induced melting**
Xiaocui Wang, J. C. Ekström, **Å. Bengtsson**, A. Jarnac, A. Jurgilaitis, Van-Thai Pham, D. Kroon, H. Enquist, and J. Larsson.
Phys. Rev. Letters 124, 105701 (2020)

- V **Repetitive non-thermal melting as a timing monitor for femto-second pump/probe X-ray experiments**
Å. Bengtsson, J. C. Ekström, Xiaocui Wang, A. Jurgilaitis, Van-Thai Pham, D. Kroon, and J. Larsson.
Structural Dynamics 7,054303 (2020)

- VI **The transition between thermal and non-thermal melting in InSb**
Åsa Bengtsson, E. Nilsson, J.C. Ekström, A. Jurgilaitis, Van-Thai Pham, D. Kroon, and J. Larsson
Manuscript in preparation

Acknowledgements

There are many people whose help has been invaluable to me while working on this thesis, and I would like to express my thanks to all of them. First of all, I would like to thank my supervisor, Prof. Jörgen Larsson, for all his guidance in matters scientific, technical and the world of academia. I would also like to thank my co-supervisor, Dr Henrik Enquist, for teaching me so much about lasers and programming, always with the greatest patience. I would like to thank everyone in the Ultrafast X-ray Science Group. Anna and Amélie, thank you for giving me a warm welcome to the group, and for showing me the ropes. Xiaocui, thank you for many enlightening discussions, many hours in the lab, and for always taking the time to share your knowledge and ideas. Carl, thank you for all your help in the lab, and for your positive attitude which made every experiment more pleasant. Eric, thank you for many enriching discussions, both scientific and non-scientific. Our conversations on music and books made long nights of data acquisition that much more fun. Thank you also to Chien-Ming and Amit, Armand, Rebecca, Erik and Blake.

I would like to thank the whole team at the FemtoMAX beamline. Special thanks to Andrius for patiently sharing his knowledge on all aspects of X-ray diffraction experiments (and for sometimes laughing at my jokes!). A big thank you to Thai and David for working tirelessly during the experiments. Thank you also to Helen and Stefano for their help during the experiments.

I would like to thank my family for their continuous support; I could not have done this without you. Special thanks to my dad for sparking my interest in science. My thoughts are perfectly captured by the best band in the world:

*“The fact is . . .
no matter how closely I study it,
no matter how I take it apart,
no matter how I break it down,
it remains consistent.
I wish you were here to see it.”*

- King Crimson, Indiscipline

Popular Scientific Summary

The light from a laser can be used to both influence and investigate a material. Ultrashort laser pulses can be used to deposit large amounts of energy in a material in a very short time. This energy is sufficient to cause structural changes in the material. A solid material can melt, and new structures can form. It is interesting to study these effects not only to increase our basic knowledge of physics, but also to develop new ways of manufacturing materials.

The study of these kinds of phenomena requires a “yardstick” of the same order of magnitude as the atomic structures in question. X-rays are electromagnetic radiation with wavelengths of the same order of magnitude as the interatomic distances in solids, and can therefore be used to study structural changes in materials. When X-rays meet a material they will be diffracted, giving rise to a pattern that can be recorded in a detector. This is called a diffraction pattern, and provides a map over the positions of the atoms. Each X-ray pulse gives a snapshot of the structure, and these are combined to form a film that shows the structural changes. These experiments place high demands on both the lasers and the X-rays used. Synchrotron facilities, such as the MAX IV Laboratory in Lund, have made it possible to generate high intensity, ultrashort pulses of X-ray light.

The work presented in this thesis has focused on two phenomena, namely pressure waves and melting. The energy from a laser pulse can generate high pressure waves in a material. This has been studied in graphite and indium antimonide. The laser energy heats the material in a localized region causing a change in the density of the material. This strain propagates as a wave through the material, and may result in a very high pressure. In one experiment presented in this thesis, a laser-induced strain wave was generated in graphite, resulting in a pressure high enough for the formation of diamond. In another experiment, strain waves were used to change the way in which the material reflects X-ray light, which can be used to create very short X-ray pulses.

During a normal melting process, so-called thermal melting, the material changes from solid to fluid through strong atomic vibrations. When an ultrafast laser pulse hits a material, a process called non-thermal melting can take place instead. The electrons in the material are excited into a state such that the atoms no longer hold together, and start to move away from each other. This happens in just a few hundred femtoseconds (10^{-15} s). Part of the work presented in this thesis was concerned with mapping how the atoms move during the non-thermal melting process. By following the melting process in the semiconductor material

indium antimonide it was possible to show that the motion of the atoms was determined by their vibrational energy at the moment of laser excitation.

Populärvetenskaplig sammanfattning

Ljuset från en laser kan användas för att både påverka och undersöka ett material. Ultrakorta laserpulser kan användas för att deponera stora mängder energi till ett material på mycket kort tid. Energin som tillförs via laserljus är tillräcklig för att åstadkomma strukturella förändringar hos materialet. Ett fast material kan smälta, och nya strukturer kan bildas. Dessa effekter är intressanta att studera både för att öka kunskapen om grundläggande fysik, och för att de kan ge upphov till nya sätt att tillverka material.

För att undersöka dessa fenomen krävs en måttstock av samma storleksordning som de atomstrukturer som ska mätas. Röntgenljus är elektromagnetisk strålning med en våglängd i samma storleksordning som de interatomära avstånden i ett fast material, och kan därför användas för att undersöka strukturella förändringar i dessa material. Röntgenljus som skickas mot ett material böjs från atomlagerna i detta materialet, och ger upphov till ett mönster som kan fångas av en detektor. Detta mönster, ett så kallat diffraktionsmönster, är en karta över atomernas positioner. För att följa hur ett material förändras över tid används korta pulser av röntgenljus. Varje puls ger en ögonblicksbild av strukturen, och när de sätts ihop i en sekvens resulterar det i en film som visar de strukturella förändringarna. För att utföra dessa experiment ställs höga krav på både lasrar och röntgenljus. Synkrotronljusanläggningar, såsom MAX IV i Lund, har gjort det möjligt att generera högintensiva, ultrakorta pulser av röntgenljus.

I detta arbete har främst två fenomen undersökts: tryckvågor och smältning. Energin från en laserpuls kan ge upphov till kraftiga tryckvågor i ett material. Detta har undersökts i grafit och indiumantimonid. Energin från en laserpuls värmer materialet på en begränsad plats och ändrar och denna töjning fortplantar sig som en våg genom materialet. Vågen medför att ett högt tryck uppstår inuti materialet. I ett experiment, gav en laserinducerad tryckvåg upphov till ett tryck som är tillräckligt högt för att diamant ska formeras. I en annan mätning användes tryckvågor för att förändra hur materialet reflekterade röntgenljus, vilket kan användas för att skapa mycket korta röntgenpulser.

Under en vanlig smältningsprocess, så kallad termisk smältning, går materialet från fast till flytande genom att atomerna vibrerar så kraftigt att de inte längre hålls ihop. När ett material träffas av en ultrasnabb laser kan istället en process som kallas icke-termisk smältning ske. Elektronerna i materialet exciteras till tillstånd som inte längre tillåter atomerna att binda till varandra, och atomerna börjar röra sig ifrån varandra. Detta sker på bara några hundra femtosekunder

(10^{-15} s). En del av arbetet som presenteras i denna avhandling har ägnats åt att kartlägga hur atomerna rör sig under den icke-termiska smältprocessen. Genom att följa smältprocessen i halvledarmaterialet indiumantimonid var det möjligt att visa att atomernas rörelser bestäms utav den rörelseenergi de har från början, vid ögonblicket då lasern träffar.

Part I

Overview

Chapter 1

Introduction

X-rays are electromagnetic waves with wavelengths similar to interatomic distances, and can thus be used to investigate the structures of solids on the atomic level by studying the way in which the material diffracts them. The development of synchrotron radiation facilities, which generate intense X-ray pulses, has made it possible to perform such studies. The short pulse duration enables the course of structural changes in a material to be monitored in real time, revealing the temporal evolution of the fundamental processes taking place. The subject of atomic motion in materials is called structural dynamics, and experiments that employ X-ray pulses in order to study this are called time-resolved X-ray diffraction experiments. Studies of structural dynamics reveal the fundamental properties of matter, and are of interest in both basic and applied research.

Femtosecond lasers can be used to deposit large amounts of energy in a material in a very short time. This can result in different phenomena, depending on the material and laser fluence. The main focus of this work was on melting and strain generation in graphite and indium antimonide . When a sample is irradiated by a laser pulse, the energy is first deposited in the electron system, which then equilibrates with the lattice, causing heating of the material. At fluences above the melting threshold, the material undergoes a phase transition from solid to liquid. At even higher fluences, excitation of the valence electrons to the conduction band causes the atoms to break apart on the sub-picosecond timescale, so-called non-thermal melting. Laser irradiation can also induce strain in a material. Heating a sample, above or below the melting threshold, induces stress in the material, which is released by the generation of a strain wave. The high pressure related to such a strain wave can be sufficient to induce phase transitions in a material.

The high X-ray flux and short pulse durations available at facilities such as the FemtoMAX beamline at the MAX IV Laboratory in Lund, which delivers 10^7 photons in pulses of 100 fs duration, are needed for these kinds of studies. However, several technical challenges must be overcome in order to perform such experiments. The ultrafast phenomena presented in this thesis can also be used to address some of these challenges. One example is the need for precise determination of the relative timing of the pump laser and X-ray probe, where non-thermal melting in semiconductors can be useful as a diagnostic tool.

The aim of the studies presented in this thesis was to study ultrafast laser-induced phenomena in solids using time-resolved X-ray diffraction, in order to gain a deeper understanding of these fundamental processes and the ways in which they can be used for technological advances.

Chapter 2 gives an overview of the materials studied in this work, and the light sources used to induce and study these effects. Chapter 3 covers the light-matter interactions involved in the studies presented in this thesis, such as heating and strain generation. The principles of X-ray diffraction and X-ray radiation generation are given in Chapter 4, together with an overview of the FemtoMAX beamline, at which most of the experiments described in this thesis were conducted. Chapter 5 describes how X-rays have been used to probe lattice dynamics in the experiments described in this thesis, and some of the practical considerations required. Chapters 6 and 7 describe the experiments performed during this work. Chapter 6 describes the experiments performed to elucidate the fundamental processes of strain generation and non-thermal melting, while Chapter 7 presents the experiments geared towards developing applications that are relevant at synchrotron radiation facilities. A summary and outlook are given in Chapter 8.

Chapter 2

Matter and Light

2.1 Matter

Matter is a very broad term, covering everything in the universe made up of particles. It can take solid, liquid or gaseous form. The work described in this thesis was concerned with solid materials in which the atoms are arranged in a periodic pattern. These materials are called crystals, as opposed to amorphous materials which lack order. Crystal structures can be described by their unit cell, i.e., the smallest volume that is repeated in the structure, and the positions of the atoms within this unit cell. Figure 2.1 shows an example of a crystal structure in two dimensions.

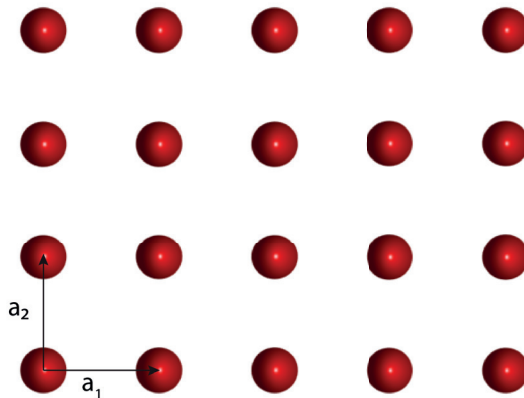


Figure 2.1: A two-dimensional crystal, where a_1 and a_2 are the crystal axes.

The crystal axes a_1 and a_2 (and a_3 in three dimensions) are the vectors that describe how the unit cell is translated. In X-ray diffraction, the crystallographic planes are of interest. A crystallographic plane is defined by three integers (h , k and l), called the Miller indices. The set of parallel planes where one plane intercepts the points a_1/h , a_2/k and a_3/l , and the nearest intercepts the origin, are called the (hkl) planes. The (112) planes in a cubic crystal structure are depicted in Figure 2.2, as an example.

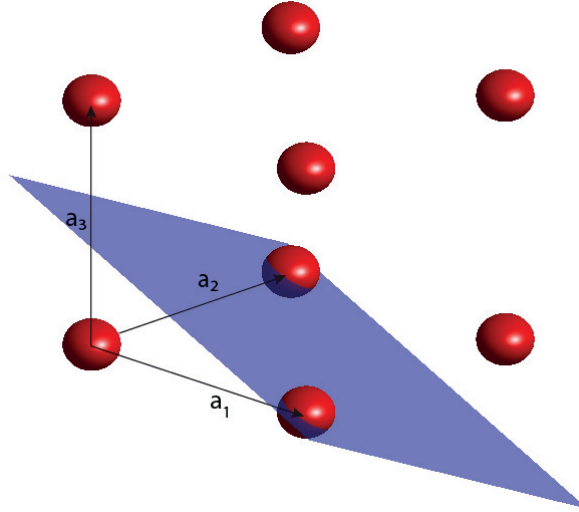


Figure 2.2: A three-dimensional crystal. The (112) plane (shaded purple) intercepts the points a_1 , a_2 and $a_3/2$.

In the work described in this thesis, mainly two materials were studied: graphite and indium antimonide (InSb). Graphite is one of the naturally occurring forms of carbon. The atoms are arranged in planes, where the atoms within a plane are covalently bound. The planes are held together by weak van der Waals bonds. This means that graphite can be relatively easily cleaved into very thin samples consisting of just a few atomic layers[1]. The 2D material graphene consists of a single layer of graphite. Due to its structure, graphite is highly anisotropic regarding both its thermal and acoustic properties[2]. Graphite is a very important material, it is for example used in lithium ion batteries[3]. The crystal structure of graphite is commonly described in the hexagonal lattice system, and is depicted in Figure 2.3.

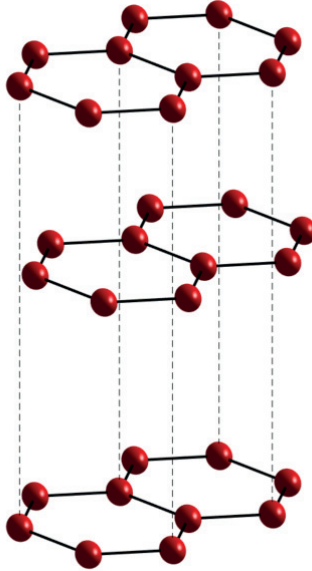


Figure 2.3: The hexagonal crystal structure of graphite. The atoms within a plane are held together covalent bonds. The bonds between the layers are weak van der Waals bonds.

The graphite sample studied in the experiment described in Paper III was a single crystal of natural graphite. Graphite also exists in other forms, such as synthetically made, highly oriented pyrolytic graphite. Papers IV and V describe studies on InSb. This is a III-V semiconductor material with a narrow bandgap of 0.17 eV, and is commonly used for applications involving the infrared region of the spectrum[4, 5, 6]. The crystal structure that is stable under ambient conditions is the zincblende structure, which is shown in Figure 2.4.

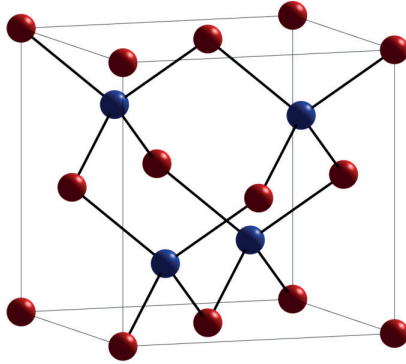


Figure 2.4: Unit cell of the zincblende structure of InSb. The crystal structure consists of tetrahedrons and the atoms are held together by covalent bonds.

2.2 Light

In the experiments performed in this work, optical lasers and X-ray beams were used in what is called pump/probe experiments. The laser beam used for excitation is called the pump beam, and the X-ray beam used for the observations is called the probe beam. Pulsed lasers with wavelengths of 800 nm were used to deposit large amounts of energy in a sample on an ultrafast timescale with the purpose of exciting the atom to elicit a specific event, such as melting. X-ray radiation was used as an observational tool. As the wavelength of X-rays is similar to the interatomic distances in crystals, X-ray photons can be used to measure structural changes within a material. The process of generating X-ray radiation, and the way in which X-ray diffraction is used to analyse atomic structures are covered in Chapter 4 and 5. A brief introduction to X-ray diffraction is given below, together with an overview of the laser systems used to induce light-matter interactions.

2.2.1 The pump laser

The samples studied in this work were pumped by ultrashort pulse lasers with a central wavelength of 800 nm. This corresponds 1.5 eV, which is sufficient to excite InSb over the bandgap. The laser systems used include amplifiers capable of producing several mJ of energy per pulse, which is high enough to significantly alter the structure of the materials.

2.2.2 The X-ray probe

An X-ray beam refracted from a crystalline material can be described as the sum of reflections from the crystallographic planes. When the X-ray beam is reflected in phase by the different planes, constructive interference leads to a peak in the diffraction intensity. The condition for constructive interference is expressed in Bragg's law[7]:

$$n\lambda = 2d \sin \theta \quad (2.1)$$

where n is the order of diffraction, λ is the wavelength of the X-rays, d is the interplanar distance and θ is the angle between the crystallographic plane and the incident beam. The parameters are indicated in Figure 2.5.

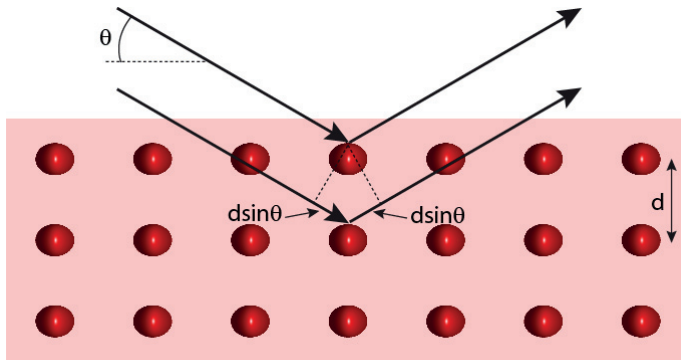


Figure 2.5: Schematic illustration of Bragg's law. The difference in distance travelled by the two rays is $2d \sin \theta$. This must correspond to an integer number of wavelengths to give rise to constructive interference.

When a material undergoes structural changes, such as compression or expansion, or when the order is lost, this will affect how the Bragg condition is met.

Chapter 3

Light-Matter Interactions

In essence, the experiments conducted within the scope of this thesis fall into two categories of light-matter interactions: 1) the phase transition from the solid to the liquid phase, i.e. melting, and 2) the generation of strain. Both these phenomena can be elicited by heating. This chapter describes the light-matter interactions that were studied in this work.

3.1 Heating

Heating can take place in many different ways. It can be achieved on an ultrafast timescale by the use of short laser pulses that deposit their energy in the sample. Upon laser excitation, the energy from the laser is first deposited in the electron system, and is then transferred to the lattice via electron-phonon coupling[8]. Heat transfer in the sample depends on the strength of the electron-phonon coupling. If a material has strong electron-phonon coupling, the energy in the electron system is transferred rapidly to the lattice, heating it quickly. However, in the case of weak electron-phonon coupling, the electrons are able to travel further into the sample before equilibrating with the lattice, and heating occurs down to a greater depth.

The Two-Temperature Model can be used in some cases to model heating[9]. This model treats the lattice and the electrons as two different systems with temperatures T_e and T_l , which equilibrate after excitation due to electron-phonon coupling. The Two-Temperature Model is expressed in Eq. 3.1:

$$\begin{aligned}
A_e T_e \frac{\delta T_e}{\delta t} &= \frac{\delta}{\delta z} \left(k_e \frac{T_e}{T_l} \frac{\delta T_e(t, z)}{\delta z} \right) - G \times (T_e(t, z) - T_l(t, z)) + S(t, z), \\
C_l \frac{\delta T_l(t, z)}{\delta t} &= G \times (T_e(t, z) - T_l(t, z))
\end{aligned}
\tag{3.1}$$

where A_e and k_e are the electronic heat capacity and electronic thermal conductivity, G is the electron-phonon coupling factor, S is the power deposited by the laser and C_l is the lattice heat capacity. The course of heating can involve interactions between different phonon modes. It has been observed in graphite that the electron system couples with optical phonons, which then couple to acoustic phonons[10]. The process of heating the lattice will then take the form of a system of coupled equations, including both the electron-phonon coupling time and the coupling time between optical and acoustic phonons:

$$\begin{aligned}
\frac{\delta E_e}{\delta t} &= -\frac{E_e}{\tau_{eo}} \\
\frac{\delta E_o}{\delta t} &= \frac{E_e}{\tau_{eo}} - \frac{E_o}{\tau_{oa}} \\
\frac{\delta E_a}{\delta t} &= \frac{E_o}{\tau_{oa}}
\end{aligned}
\tag{3.2}$$

where E_e , E_o and E_a are the energies in the electron, optical phonon and acoustic phonon system, respectively, and τ_{eo} and τ_{oa} are the coupling times between the electrons and optical phonons, and between the optical and acoustic phonons. The heat profiles in the electron and phonon systems described by Equations 3.2 are shown Figure 3.1.

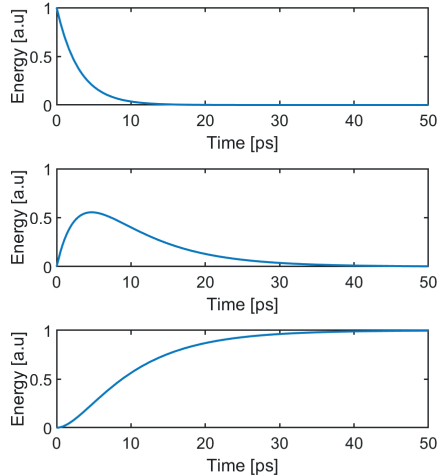


Figure 3.1: : The heat source profiles in the electron (top), optical (middle) and acoustic phonon systems (bottom) with coupling times $\tau_{eo} = 3$ ps and $\tau_{oa} = 8$ ps.

3.2 Melting

The melting process encountered in everyday life is thermal melting, a process in which the thermal vibrations of the atoms in a solid become so large that the interatomic bonds are broken. This can easily be achieved by laser irradiation if sufficient energy is deposited to increase the temperature to the melting point and for phase transition. When melting is induced by an ultrashort laser pulse, the melting time is of the order of picoseconds, and depends on the electron-phonon coupling strength and the intensity of the laser pulse, as described in the previous section.

The possibility of non-thermal melting processes was first suggested in 1979, after observations during laser annealing of Si that were inconsistent with a purely thermal process[11]. The atoms in a solid semiconductor are held together by the bonding orbitals of the electrons in the valence band. If enough of these electrons are excited into the conduction band the potential landscape of the crystal becomes significantly perturbed. The interatomic bonds are then broken, resulting in a transition from the solid to the liquid phase[12, 13, 14, 15]. It has been found that 10% of the electrons must be excited into the conduction band in order for non-thermal melting to occur[16, 17].

In 2005, Lindenberg et al. proposed the inertial model to describe the process

of non-thermal melting[18]. According to this model, upon bond-breaking, the atoms will continue to move with the velocity they had due to their thermal vibrational energy. Thus, the time taken to melt a sample should be proportional to the initial temperature of the sample. The inertial model has been contested by some theoreticians who claimed that the atomic velocities were only influenced by the shape of the potential landscape[19]. Paper IV describes an experiment performed to settle this controversy and elucidate the process of non-thermal melting.

3.3 Laser-induced periodic structures

When illuminating a material with laser radiation at fluences that can induce melting, effects will also take place at the surface. The formation of periodic structures on the surface following repetitive laser irradiation has been reported in several cases[20, 21, 22]. This is the result of inhomogeneous energy absorption due to interference between the refracted laser beam and scattered fields in the material. Figure 3.2 shows a microscope image of the ridges on a sample after laser irradiation. Although this is a surface effect, these structures have an impact on measurements below the surface. Figure 3.3 shows a schematic of the sample surface as seen from the side. As can be seen, the ripples on the sample surface result in changes in the angle of incidence of the X-ray beam. This in turn affects the probe depth of the X-rays. (The importance of X-ray probe depth in an experiment is discussed further in Section 5.4.)

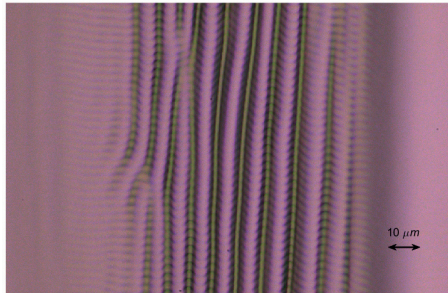


Figure 3.2: Microscope image of a sample of InSb after repeated laser irradiation.

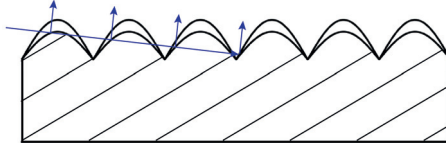


Figure 3.3: Schematic of sample surface structure after laser irradiation. As the surface is no longer flat, the X-rays will experience different angles of incidence depending on where they impinge on the sample. This affects the probe depth, and may result in a diffracted signal from deeper into the sample than expected.

3.4 Strain generation

When a sample is heated by a laser, pressure is built up as a result of the change in the density of the material. This pressure gives rise to a strain wave travelling into the sample. Thomsen presented a model describing the strain in a solid resulting from a laser pulse[23, 24]. This model assumes that the size of the laser profile on the sample is very large compared to the sample thickness, so the system can be described as one dimensional. It is also assumed that the optical absorption depth is much less than the sample thickness. The energy deposited per unit volume at depth z is given by Equation 4:

$$W(z) = (1 - R) \frac{Q}{A\zeta} e^{-z/\zeta} \quad (3.3)$$

where Q is the pulse energy, R is the reflectivity, A is the illuminated area and ζ is the absorption length of the material. The resulting increase in temperature is given by:

$$\Delta T(z) = \frac{W(z)}{C} \quad (3.4)$$

where C is the specific heat per unit volume. The rise in temperature causes thermal stress, which is then released as a strain wave. Since the temperature increase is dependent only on the depth, so is the stress. Solving the equations of elasticity for the initial conditions of zero strain everywhere, and zero stress at the surface at all times, gives a strain wave in the direction perpendicular to the surface:

$$\eta_{33}(z, t) = (1 - R) \frac{QB}{A\zeta} \frac{1 + nu}{1 - nu} \left[e^{-z/\zeta} \left(1 - \frac{1}{2} e^{-vt(\zeta)} \right) - \frac{1}{2} e^{-|z-vt|/\zeta} \text{sgn}(z - vt) \right] \quad (3.5)$$

where B is the bulk modulus, ν is Poisson's ratio and v is the speed of sound in the material. A solution to Equation 6 is shown in Figure 3.4. The solution is comprised of two parts. The first term on the right-hand side of the equation is the static strain due to thermal expansion, while the second is a strain wave travelling into the sample at the speed of sound.

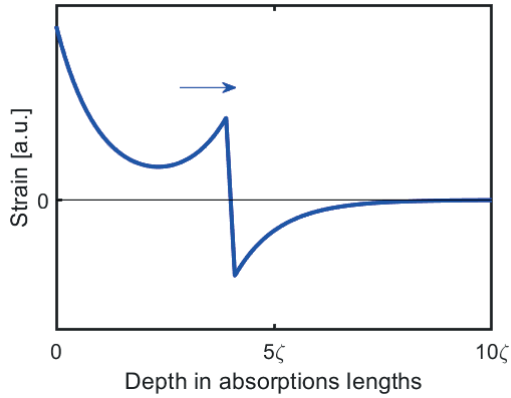


Figure 3.4: : A strain wave propagating in material after laser irradiation. Positive strain occurs at the surface, and a wave comprised of a positive and negative part travels into the material. Note that the depth is given in terms of the absorption length of the material (ζ)

A similar description of strain was used to model a laser-induced strain wave in graphite (Paper III). As stated above, this model is only valid at a depth, z , that is small compared to the laser footprint on the sample, i.e., the near-field region, $z \sim W^2/\zeta$. The optical absorption length of graphite is $0.2 \mu\text{m}$ [25], and the laser footprint is $300 \mu\text{m} \times 300 \mu\text{m}$, which means that the model is valid in this respect. It is also assumed in the model that the increase in temperature is instantaneous. The laser pulse duration in this study was 1.2 ps. During this time, the strain wave travels a distance of 1.8 nm (using the speed of sound in graphite[26]), which is very short compared to the length of the strain wave, so this can be disregarded.

3.5 Large-amplitude strain

A large-amplitude strain wave was generated in graphite using a laser fluence above the damage threshold (Paper III). The surface of the graphite melted due to the high laser fluence, and the strain wave resulted from the difference in density between the solid and liquid phase. The pressure related to the strain was extracted using the bulk modulus, which describes the compressibility of the material. The pressure induced was sufficiently high to place the material in the region of the phase diagram for carbon where diamond formation is possible.

3.6 Strain in a thin film

A strain wave travelling through a material will, on encountering a boundary with a material of different acoustic impedance, be partially reflected and partially transmitted. The difference in acoustic impedance of the two materials determines the fractions of the wave that are reflected and transmitted. The reflection and transmission coefficients, R and T, are given below:

$$R = \frac{Z_2 - Z_1}{Z_2 + Z_1}, \quad T = \frac{B_1}{B_2} \frac{2Z_2}{Z_2 + Z_1}, \quad Z_i = \rho_i v_i \quad (3.6)$$

where Z_i , B_i , ρ_i and v_i denote the acoustic impedance, bulk modulus, density and velocity of sound for the two materials. Figure 3.5 shows a strain wave reflected at a boundary. The indices $i = 1$ and $i = 2$ refer to the propagating and transmission materials, respectively. The amplitude of the reflected wave increases with increasing disparity between the impedance of the materials. When the propagating wave encounters a boundary with a material of lower impedance, it undergoes a phase shift of π , however, if the second material has a lower acoustic impedance there will be no phase shift. If the propagating material is a thin film, there will be multiple reflections of the wave at both boundaries as the wave travels back and forth in the film.

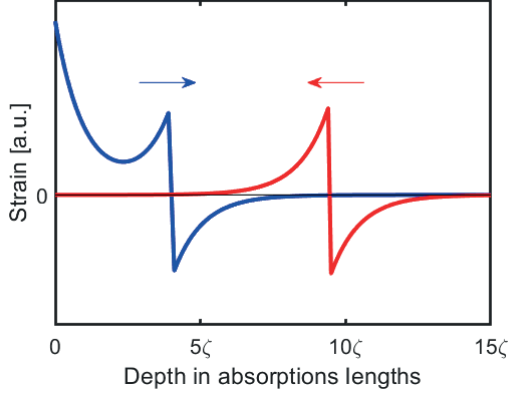


Figure 3.5: Strain wave reflected at a boundary. The blue curve shows the strain wave propagating into the sample. The red curve shows the strain wave after reflection at a boundary. In the case shown here, the second material is vacuum, so the amplitude of the reflected wave is unchanged, and there is a phase shift of π .

3.7 Modulating the phonon spectrum

Phonons are quantized modes of lattice vibrations in a material. As phonon modes have a certain periodicity, it is possible to probe them with X-rays through a small adjustment of the Bragg condition. Paper I describes the development of an X-ray switch based on a photo-acoustic transducer. The functionality of the X-ray switch was based on the ability to modify the phonon spectrum using a laser-generated strain wave.

The phonon spectrum of a material can be modulated by a strain wave travelling through the material[27, 28]. The previous section described how a strain pulse in a thin film will be reflected back and forth between the two boundaries. If a thin film is deposited on top of a thicker bulk sample, a strain pulse will be transmitted into the bulk material each time the strain pulse in the film reflects off the film/bulk boundary. The strain pulse will be reflected back and forth within the film with a period $T = 2d/v$, where v is the speed of sound in the material. This will result in a strain wave in the bulk material, as shown in Figure 3.6. The strain wave can be described as a superposition of phonon modes, and will consequently have an effect on the phonon modes of the sample. The phonon modes in the bulk material will be cancelled out or enhanced depending on their period. Phonon modes with a periodicity of $m \times T$ will be enhanced when m is an odd integer, and cancelled when m is an even integer.

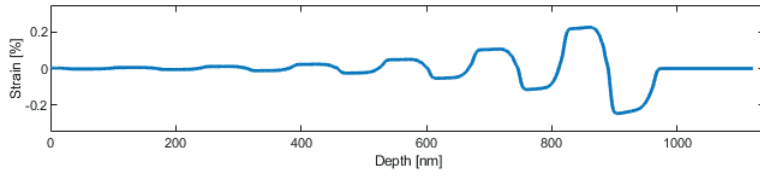


Figure 3.6: A strain wave in bulk material generated by reflections of strain pulse in thin film.

Chapter 4

Principles of X-ray Diffraction and Generation

As X-rays are electromagnetic waves with wavelengths similar to interatomic distances, they are sensitive to structural changes in matter. In X-ray diffraction experiments, elastically scattered X-ray photons are measured in order to map the structure of a crystalline material. Time-resolved X-ray diffraction experiments are among the most important when studying the structural properties of matter on the atomic scale. This section describes the principles of X-ray diffraction and how X-rays are generated. An overview of the Femto-MAX beamline is also given.

4.1 X-ray scattering

X-ray diffraction originates from scattering by the electrons of the atoms making up the material. This section describes X-ray scattering from an electron, an atom and a crystal.

4.1.1 Scattering by a single electron

Consider a free electron and an incident X-ray beam travelling along the z direction, as depicted in Figure 4.1. In the classical picture, the electric field of the X-ray beam will accelerate the electron, which will radiate in all directions in response. The intensity of the scattered X-ray beam at a position P , in the

yz-plane, is given by Eq. 4.1 [29]:

$$I = I_0 \frac{e^4}{m^2 c^4 R^2} \left(\frac{1 + \cos^2 \phi}{2} \right) \quad (4.1)$$

where I_0 is the intensity of the incident beam, e and m are the elementary charge and electron mass, R is the distance from O to P , and ϕ is the angle between the incident beam and the direction of observation. The scattered photons will have the same wavelength as the incident beam. This is unmodified Thomson scattering, and is the basis of X-ray diffraction. The expression in Equation 4.1 describes the scattering of an unpolarized incident beam. The polarization factor, $(1 + \cos^2 \phi)/2$, will be different if the incident beam is polarized.

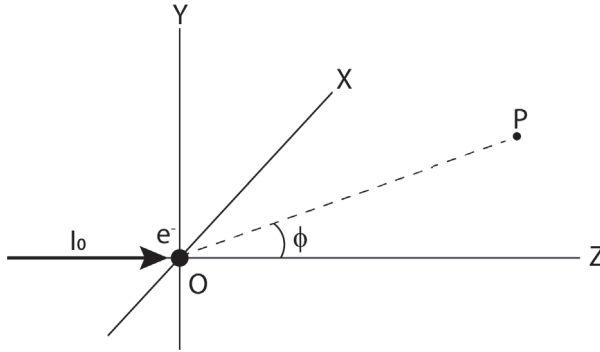


Figure 4.1: Scattering of an X-ray beam by a single electron.

4.1.2 Scattering by an atom

When calculating the intensity of the beam scattered from an atom, contributions from all the electrons must be taken into account. The amplitude of the field scattered from an atom is given by the atomic scattering factor, f , which is the sum of the scattered fields from all the electrons in the atom:

$$f(\mathbf{Q}) = \int_0^\infty \rho(\mathbf{r}) e^{i\mathbf{Q}\cdot\mathbf{r}} d\mathbf{r} \quad (4.2)$$

where \mathbf{Q} is the scattering vector, and ρ is the electron density. Scattering factors can usually be found in tables for X-ray interactions[30].

4.1.3 Scattering by a crystal: Bragg's law

Scattering from a crystal can be regarded as scattering from a series of layers of atoms that are evenly spaced by the distance d . The incident beam is scattered in phase by the atomic layers when the difference in the path length of the scattered light from different planes is an integer multiple of the wavelength. This results in sharp peaks in the scattered intensity, called Bragg peaks. The condition for constructive interference from the atomic layers, Eq. 2.1, is called Bragg's law, as described in Section 2.2.2.

4.1.4 Reciprocal space

Section 2.1 gave a description of crystalline structures in terms of the crystal axes. Describing the crystal in reciprocal space instead provides a useful and easy way to describe the crystal planes and formulate the diffraction condition. The three reciprocal lattice vectors are constructed using the crystal axes a_1 , a_2 and a_3 .

$$\mathbf{b}_1 = \frac{\mathbf{a}_2 \times \mathbf{a}_3}{\mathbf{a}_1 \cdot \mathbf{a}_2 \times \mathbf{a}_3}, \quad \mathbf{b}_2 = \frac{\mathbf{a}_3 \times \mathbf{a}_1}{\mathbf{a}_1 \cdot \mathbf{a}_2 \times \mathbf{a}_3}, \quad \mathbf{b}_3 = \frac{\mathbf{a}_1 \times \mathbf{a}_2}{\mathbf{a}_1 \cdot \mathbf{a}_2 \times \mathbf{a}_3} \quad (4.3)$$

With the help of the reciprocal lattice vector, it is possible to define a vector that describes the orientation and spacing of the crystal planes.

$$\mathbf{Q}_{hkl} = h\mathbf{b}_1 + k\mathbf{b}_2 + l\mathbf{b}_3 \quad (4.4)$$

\mathbf{Q}_{hkl} is perpendicular to the crystal plane defined by the integers h , k and l , and the absolute value is the reciprocal of the spacing between the planes. The scattering vector \mathbf{Q}_{hkl} can be used to express Bragg's law in vector form:

$$\mathbf{k} - \mathbf{k}_0 = \mathbf{Q}_{hkl} \quad (4.5)$$

where \mathbf{k}_0 and \mathbf{k} are the wave vectors of the incident and refracted beams. Bragg's law is illustrated in Figure 4.2.

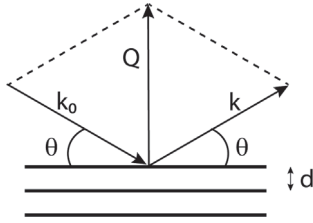


Figure 4.2: Visualisation of Bragg's law in vector form.

4.1.5 The Ewald sphere

The Ewald sphere can be used to visualise Bragg's law in vector form. A representation in two dimensions is shown in Figure 4.3. The grid represents the reciprocal space, and the sphere is constructed by drawing the incident beam so that it ends at the origin of reciprocal space. The sphere is then centred on the origin of the incident beam, and the radius is the magnitude of the wave vector \mathbf{k}_0 . Every grid point is then an hkl plane, the \mathbf{Q}_{hkl} vector of which satisfies the Bragg condition for a diffracted beam, \mathbf{k} . The angle between the two beam vectors is the scattering angle 2θ . It is easy to see how the Bragg condition can be fulfilled for different reflections by changing the angle or length of the beam vectors.

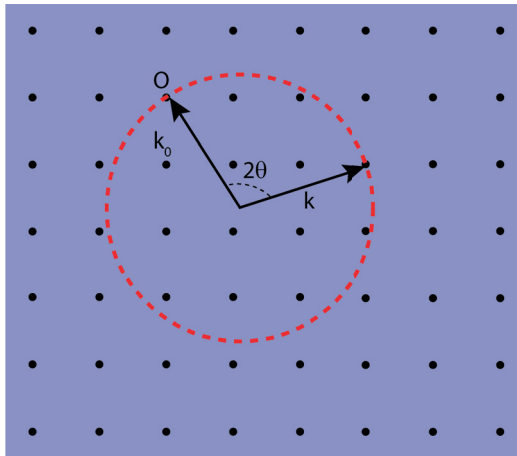


Figure 4.3: The Ewald sphere illustrated in 2D.

4.1.6 The structure factor

The relative intensities of the reflections are given by the structure factor, F , which is determined by the atomic positions and the atomic scattering factor:

$$F = \sum_n = f_n e^{(2\pi i)(\mathbf{k}-\mathbf{k}_0)\cdot\mathbf{r}_n} \quad (4.6)$$

where f_n is the atomic scattering factor. In the case of a Bragg reflection from an hkl plane, the expression takes the form:

$$F = \sum_n = f_n e^{(2\pi i)(hx_n+ky_n+lz_n)} \quad (4.7)$$

where x_n , y_n and z_n are the fractional coordinates of the atoms in the unit cell. All crystal structures can be sorted into 14 different basic structures, so-called Bravais lattices. Each type of lattice has certain symmetries that determine the intensity, or lack thereof, of certain Bragg reflections. The zincblende structure of InSb can be used as an example. The unit cell consists of four indium atoms and four antimony atoms placed according to:

In: $(0, 0, 0), (1/2, 1/2, 0), (1/2, 0, 1/2), (0, 1/2, 1/2)$

Sb: $(1/4, 1/4, 1/4), (3/4, 3/4, 1/4), (3/4, 1/4, 3/4), (1/4, 3/4, 3/4)$

Using these atomic positions in Eq. 4.7, gives the structure factor for zincblende.

$$F_{hkl} = f_{In} * (1 + e^{\pi i(h+k)} + e^{\pi i(h+l)} + e^{\pi i(k+l)}) + f_{Sb} * e^{\frac{\pi i(h+k+l)}{2}} + *(1 + e^{\pi i(h+k)} + e^{\pi i(h+l)} + e^{\pi i(k+l)}) \quad (4.8)$$

For reflections where hkl are all odd or all even this can be further simplified.

$$F_{hkl} = 4[f_{In} + f_{Sb}e^{(\pi i/2)(h+k+l)}] \quad (4.9)$$

When the indices have both odd and even values the structure factor becomes zero, and the reflection is said to be forbidden. An interesting case for InSb occurs when $h + k + l = 2(2n + 1)$, in which case the structure factor becomes:

$$F_{hkl}^2 = 16(f_{In} - f_{Sb})^2 \quad (4.10)$$

Indium and antimony have similar mass and atomic scattering factors, so the structure factor is close to zero, and the reflection is semi-forbidden. This is briefly discussed in the Outlook (Chapter 8). Similar calculations can be performed for the other crystal structures to determine which reflections are strong and which are weak.

4.1.7 Imperfect and perfect crystals

Only one reflection is indicated in Figure 2.5. However, in reality there will be other reflections of the beam. A portion of the beam will be reflected back from the surface, which will reduce the intensity of the diffracted beam. However, this is only relevant for highly regular crystals, usually called perfect crystals. The regularity of the crystal influences how the intensity of the diffracted beam scales with the number of atomic layers. For a perfect crystal, the diffraction intensity is proportional to the square of the number of layers. For an imperfect crystal, the intensity is proportional to the number of layers. The natural graphite sample used in the experiment presented in Paper III is an example of an imperfect crystal.

4.2 X-ray generation

Advancements in the field of structural dynamics rely on access to bright, short X-ray pulses, which are necessary to achieve a good signal-to-noise ratio and high temporal resolution. The work presented in this thesis included both destructive and non-destructive measurements. Data can be acquired continuously when using non-destructive measurements, and the photon flux determines the acquisition time required. Destructive measurements cause irreversible transitions in the material, and the data must be acquired in single shots, thus, the number of X-ray photons per pulse will determine the signal-to-noise ratio. Atomic motion typically takes place on the timescale of hundreds of femtoseconds or picoseconds, and the X-ray pulses must be equally short in order to capture the course of these events.

Different methods can be used to generate X-rays pulses, which result in different photon fluxes and pulse durations. Laser-plasma sources provide table-top solutions for X-ray pulse generation[31, 32]. Other, larger, facilities include synchrotron facilities based on storage rings, such as the European Synchrotron Radiation Facility (ESRF) in France and MAX IV in Sweden, and linear-accelerator-based sources, such as the FemtoMAX beamline at MAX IV. Free-

electron lasers, such as the Linac Coherent Light Source at the SLAC National Accelerator Laboratory in USA [33] and the European XFEL in Germany can also be used to produce bright, short X-ray pulses[34].

Laser plasma sources are based on the radiative electron transitions in atoms. An intense femtosecond laser pulse is focused onto a metal target, and a high-density plasma is created as the atoms in the target are ionized by the laser. After creation of the plasma, the motion of the free electrons is controlled by the laser field. The electrons are first extracted from the target, and then accelerated and directed back to the target, where they excite the inner-shell electrons of the target atoms. X-ray photons are emitted during the recombination of outer-shell electrons and inner-shell holes. The resulting X-ray pulses have a similar duration to that of the laser.

Higher-intensity X-ray pulses can be achieved using electrons accelerated in synchrotron light sources[35]. The electrons are kept in storage rings, where they travel in a circular path at relativistic speeds. Bending magnets are used to direct the electrons around the storage ring. When accelerated by a magnet the electrons emit X-rays. The energy, E_c , of the X-ray photons emitted by electrons accelerated in a magnetic field B is given by[36]:

$$E_c = \frac{3\hbar e\gamma^2 B}{2m} \quad (4.11)$$

where \hbar is the reduced Planck constant, e is the elementary charge, γ is the relativistic parameter and m is the rest mass of the electron. The relativistic parameter is defined as:

$$\gamma = \frac{1}{\sqrt{1 - \left(\frac{v_e}{c}\right)^2}} \quad (4.12)$$

where v_e is the electron velocity, and c is the speed of light. E_c is called the critical energy, and is defined such that half of the power is emitted at energies below this value, and half above. Periodic structures of dipole magnets with alternating polarity, called undulators or wigglers, are used to accelerate electrons in order to generate X-ray radiation. The Lorentz force from the alternating magnetic field causes the electrons to “wobble” in the transverse direction, and as they do they will emit radiation. The energy of the resulting radiation is given by[37]:

$$E_u = \frac{2n\gamma^2 hc}{\lambda_u e} \left(1 + \frac{K^2}{2} + \theta_e^2 \gamma^2 \right) \quad (4.13)$$

where n is the harmonic order, λ_u is the periodicity of the dipole magnets and θ_e is the angle of radiation relative to the optical axis. K is the undulator parameter, defined as in Eq. 4.14.

$$K = \frac{eB\lambda_u}{2\pi mc} \quad (4.14)$$

The electrons are collected into bunches in the storage ring, and as an electron bunch moves through the undulator, an X-ray pulse of the same duration as the length of the bunch is generated, typically around 100 ps.

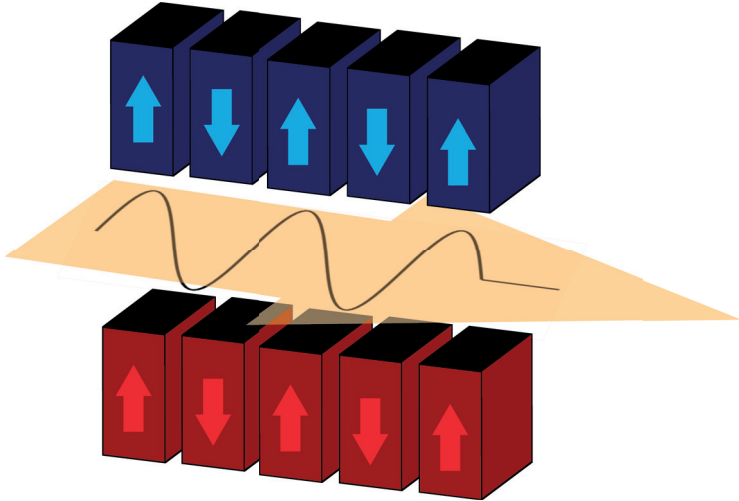


Figure 4.4: An undulator is comprised of alternating magnets that cause wiggling of the electrons.

Extremely high pulse energies and short pulse durations, on the order of tens of femtoseconds, can be achieved with free-electron lasers. Free-electron lasers make use of very long undulators. Again, the alternating magnetic field will cause the electron bunches to emit radiation. However, in contrast to storage rings, the radiation will co-propagate with the electrons. The magnetic field from the emitted radiation will cause the electrons to form microbunches, which then continue to emit photons coherently.

4.3 The FemtoMAX beamline

Short X-ray pulses are needed to carry out measurements with high temporal resolution. The FemtoMAX beamline at the MAX IV Laboratory in Lund, Sweden, is dedicated to providing ultrashort, bright X-ray pulses for time-resolved pump/probe X-ray diffraction experiments.

Four of the experiments included in this thesis were performed at the FemtoMAX beamline at the MAX IV Laboratory. The linear accelerator that provides electrons for the storage rings is also used to provide electrons for the generation of X-ray pulses for the FemtoMAX beamline. The electrons are produced with an electron gun by laser excitation of a cathode that ejects electrons. The X-ray photons are produced by two undulators, which are able to generate X-ray radiation in the energy range 1.8 to 13 keV. Two kinds of monochromators can be used to produce monochromatic radiation: multilayer monochromators with a bandwidth of 10^{-2} , and double crystal monochromators with InSb and Si crystals, with bandwidths of $2 \cdot 10^{-4}$ and $4 \cdot 10^{-4}$, respectively.

The laser system at the FemtoMAX beamline includes a Ti:sapphire amplifier that can deliver 13 mJ pulses at a wavelength of 800 nm. An optical parametric amplifier can be introduced to produce radiation at wavelengths ranging from 0.2 to 10 μm . The laser system is synchronized to the X-ray beam by locking the laser oscillator to the RF signal from the linear accelerator.

Chapter 5

X-ray Diffraction Experiment Techniques

In all the experiments described in this thesis, the effects were induced by an ultrafast laser in the optical wavelength region. In order for the experiments to yield useful results, the pump laser and the X-ray probe must be overlapped in both time and space. Although the laser and X-rays are synchronized, there is always inherent jitter, and the actual arrival times of the pump laser and X-ray probe on the sample must be determined. The two beams must also overlap in space, i.e., interact with the same part of the sample. This applies to both the surface area on the sample, as well as the depth in the sample. This section describes the practical aspects of pump/probe experiments, and how they should be set up in order to achieve meaningful results.

5.1 Symmetric and asymmetric crystals

A crystal can be cut symmetrically or asymmetrically with regard to a certain crystallographic plane. In a symmetrically cut crystal, the crystal planes of interest are oriented parallel to the surface, while in an asymmetrically cut crystal they are not. Figure 5.1 illustrates the two cases. The kind of crystal used will affect the experimental geometry, and the data analysis. InSb can be used as an example. The Bragg angle for the (111) reflection at 3.5 keV is 28° , and so it would be impossible to fulfil the diffraction condition in an experiment with grazing incidence geometry. Using a sample cut at an angle of 30° allows the 111 Bragg peak to be probed in a grazing incidence geometry.

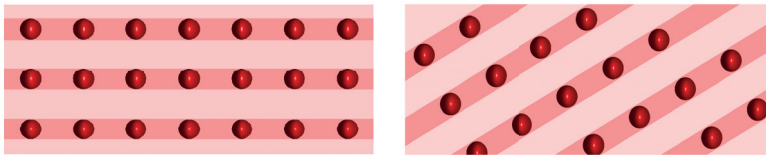


Figure 5.1: Illustration of a crystal cut symmetrically for the indicated crystallographic plane (left), and the asymmetric case (right).

The cutting angle also influences the data analysis as the X-ray beam will be attenuated differently in the two cases. For a symmetrically cut sample, the X-rays will travel the same distance before and after diffraction, and will be attenuated by the same amount in both directions. In a grazing incidence geometry, the diffracted beam travels a much shorter distance through the sample than the incidence beam, so the attenuation of the diffracted beam can be disregarded. This is illustrated in Figure 5.2.

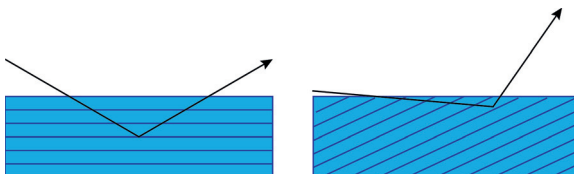


Figure 5.2: Path of the X-ray beam in a symmetric (left) and an asymmetric (right) crystal. In the symmetric crystal, the original and diffracted beam will travel the same distance through the material. In the asymmetric case, the diffracted X-ray beam travels a comparatively short distance through the material, and its absorption can therefore be neglected. An asymmetrically cut crystal enables experiments to be performed in a grazing incidence geometry, as the cut angle can be chosen in order to satisfy the Bragg condition.

5.2 Coplanar and non-coplanar geometry

An X-ray diffraction experiment can be performed in a coplanar or non-coplanar geometry. The experimental geometry is defined by the plane spanned by the incident and diffracted beam, and the sample surface normal. If the normal is parallel to the plane, the geometry is called coplanar, otherwise, it is non-coplanar. In order to fulfil the diffraction condition for a scattering plane that is not parallel to the surface of the sample, it is necessary to consider the rotation of the sample around the surface normal, i.e. the azimuthal angle. When adjusting the azimuthal angle of an asymmetric sample, the angle between the crystal plane normal and the incident X-ray beam also changes. The non-coplanar geometry can be particularly useful when studying changes in the crystal structure, as described in Paper III. Changing the distance between crystalline planes will result in a change in the Bragg angle, so the angle of incidence of the beam must

be changed in order to follow the Bragg peak. In a non-coplanar geometry, a smaller adjustment in azimuthal angle is sufficient to fulfil the diffraction condition, so the Bragg peak can be continuously captured without changing the experimental geometry.



Figure 5.3: Left: Coplanar geometry, where the surface normal is parallel to the plane spanned by the incident and refracted beams. Right: Example of a non-coplanar geometry.

5.3 Determining the angle of incidence

The non-thermal melting experiments were performed in a grazing angle geometry, where it is especially important to determine the angle of incidence correctly, since the probe depth is very sensitive to this. The angle of incidence is set using a tilt motor stage, however the 0° position needs to be calibrated carefully for each experiment. The procedure for doing this is to capture the direct beam and the specular reflection at the same time. Figure 5.4 shows the experimental set-up used to determine the angle of incidence. The sample angle is varied using a tilt motor stage, and images of the direct beam and specular reflection are captured. The distance between the direct beam and the specular reflection on the detector is determined as a function of the sample tilt motor stage position. When the angle of incidence is 0° , the distance between the direct beam and the specular reflection is zero. The graph in Figure 5.4 shows the results from a measurement of the angle of incidence. Extrapolation of the data indicates the motor stage position at which the distance between the direct and specular beams is zero, and thus where the angle of incidence is 0° .

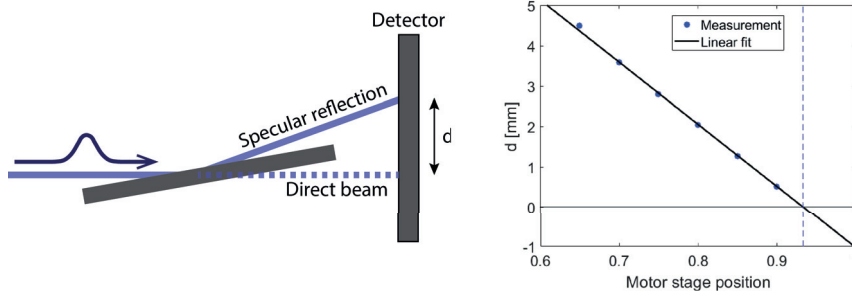


Figure 5.4: Schematics illustrating the measurement of the angle of incidence (left). Results of such a measurement (right). In this measurement the angle of incidence is 0° when the motor stage position is 0.93.

5.4 Probe depth

The attenuation of the X-ray beam by a material is described by the Beer-Lambert Law:

$$I(z) = I_0 e^{-\mu z} \quad (5.1)$$

where I_0 is the intensity of the incident beam, μ is the attenuation coefficient of the material and z is the depth in the sample. The probe depth varies with the angle of incidence, and should be considered bearing in mind the absorption depth of the pump laser. The experiments presented in Papers IV and V, which are concerned with melting, were set up in a grazing angle of incidence geometry, so the probe depth was very shallow, and the X-rays only probed the molten region of the sample. For experiments performed in a grazing incidence geometry it is also important to consider refraction, which will alter the angle of incidence inside the sample. In the experiments presented in Papers I and III, the angle of incidence was greater in order to probe the strain wave generated below the depth where the laser energy is absorbed.

5.5 Space-time mapping for high temporal resolution

The evolution of a process over time can be studied with high temporal resolution in a single X-ray shot by carefully choosing the experimental geometry. Figure 5.5 shows the experimental set-up used for the non-thermal melting experiments described in Papers IV and V. Due to the difference in angle between

the laser pump and X-ray probe, the difference in the time of arrival of the laser pump and X-ray probe will differ at different sample positions. Diffracted X-rays from the different sample positions are in turn captured at different positions on the detector. In this way, the spatial extension of the detector becomes a time axis.

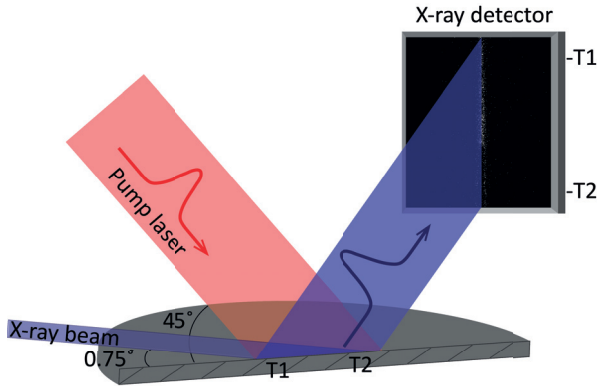


Figure 5.5: Schematic view of experimental set-up for the non-thermal melting experiments. The relative timing between the laser pump and X-ray probe will differ at sample positions T1 and T2 due to the difference in the angle of incidence of the two beams. Diffracted X-ray signals from sample positions T1 and T2 will be captured at different positions on the detector, which allows the temporal evolution of the process to be captured in one image.

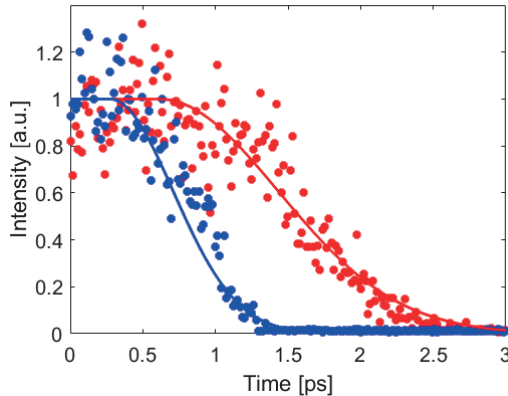


Figure 5.6: Results of a spectral smearing measurement. The blue curve shows the results of the DCM measurement, and the red curve the multilayer monochromator measurement. The comparatively small bandwidth of the DCM results in a much sharper decrease in signal.

The temporal resolution of this method depends on the difference in angle between the laser and X-ray beam and the pixel pitch of the detector. The

bandwidth of the X-ray beam must also be considered, since this translates into divergence of the diffracted beam, leading to smearing in the spatial dimension, and thus in the temporal trace. The magnitude of this spectral smearing can be measured by cutting the X-ray beam with an opaque object, and observing the steepness of the decrease in signal on the detector. Figure 5.6 shows the results of two measurements, one where a multilayer monochromator with a bandwidth of 1% was used, and the other where a double crystal monochromator (DCM) with a bandwidth of 0.01 %, was used with the beam. The effect of the bandwidth on the temporal resolution can be clearly seen. The DCM was chosen during the non-thermal melting experiments, as this provides an X-ray beam able to resolve events of a few hundred femtoseconds, and the multilayer monochromator does not.

5.6 Measuring disorder

The intensity of a Bragg reflection is dependent on the precise periodicity of the atoms. When the atoms move incoherently, this has an adverse effect on the diffracted X-ray intensity. The thermal motion of atoms in a crystal can thus be studied by measuring the intensity of a Bragg reflection. The Debye-Waller formalism describes how the thermal motion of atoms in a material attenuates X-rays:

$$I(t) = I(0)e^{-Q^2\langle u^2(t)\rangle/3} \quad (5.2)$$

where Q is the reciprocal lattice vector of the probed Bragg reflection and $u(t)$ is the displacement of the atoms. $I(0)$ is the initial intensity of the Bragg reflection from an unperturbed crystal. The average mean square displacement of the atoms is given by:

$$\langle u^2(t) \rangle = v_i^2 t^2 \quad (5.3)$$

where v is the initial velocity, and t is time. Debye-Waller formalism is usually associated with thermal processes, however Lindenberg et al.[16] suggested that it could also be used when modelling the disorder caused by non-thermal melting.

5.7 Measuring strain

In a strained material, the positions of the atoms will differ from the nominal, thus affecting the scattering conditions. Figure 5.7 shows a crystal with both compressive and expansive strain.

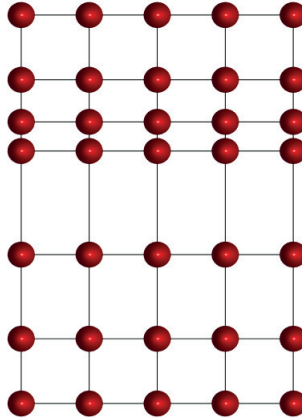


Figure 5.7: Figure 22: Schematic view of a strained crystal structure.

The strain is related to the change in momentum transfer vector through:

$$S = \frac{Q - Q'}{Q} \quad (5.4)$$

where S is the magnitude of the strain and Q and Q' are the unstrained and strained momentum transfer vectors. The magnitude of the strain can thus be deduced by adjusting the experimental geometry and observing the change in position of the diffracted X-ray beam on the detector, which is related to the change in Q . The width of the strained part of the material can be deduced from the strength of the reflection, as the diffracted X-ray intensity is related to the number of diffracting atomic layers.

Chapter 6

Strain Generation and Melting

Ultrashort laser pulses can induce structural changes in materials. This section presents the work carried out to investigate two different kinds of dynamics. Measurements were performed on graphite to investigate the effect of large-amplitude strain waves, while InSb was used to map the processes of thermal and non-thermal melting.

6.1 Large-amplitude strain wave in graphite

Graphite and diamond are the two naturally existing allotropes of carbon[38]. Their structures differ due to different bond hybridization, and thus their material properties differ. Diamond is formed naturally under extreme temperature and pressure. There are also reports of nanoscale diamonds forming upon ultrafast laser irradiation[39, 40, 41]. It has also been suggested that diamonds can be formed from graphite using large shock waves[42].

In this work (Paper III), the energy of short, intense laser pulses was used to generate a large-amplitude strain wave in a graphite sample to investigate the effects of high pressure on the crystal structure. The resulting strain wave, which could be important in driving a phase transition, was measured and characterised. A pulsed laser was used to generate the strain wave. The laser pulse melts the upper layers of the graphite sample, and the transition from solid to liquid causes stress in the sample. This stress is released by the generation of a compressive strain wave, which propagates into the sample. The footprint of the laser is very large, $300\ \mu\text{m}$ by $300\ \mu\text{m}$, compared to the depth to which the strain wave travels, so this can be described as a one-dimensional problem, as

explained in Section 3.4.

The strain wave was characterised by observing the evolution of the (103) Bragg reflection over time. The generation of a compressive strain wave means that the distance between the crystalline planes will be decreased, so the momentum transfer vector for this reflection is increased. This will result in a spatial shift of the diffracted X-ray beam. The strain wave can thus be monitored by following the Bragg reflection on the detector.

This experiment was conducted at the ID09 beamline at the ESRF. The energy of the X-ray beam was 15 keV, and the corresponding bandwidth 2.2%. Laser pulses from a Ti:Al₂O₃ laser, with a pulse duration of 1.2 ps and central wavelength at 800 nm, were used to pump the sample, which was a single crystal of natural graphite. The experiment was performed above the ablation threshold.

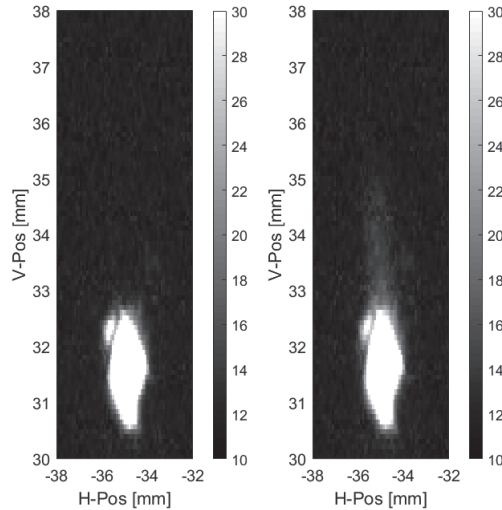


Figure 6.1: Bragg reflection captured without laser irradiation (left) and 200 ps after laser irradiation (right). The "tail" in the right diffraction spot indicates strain in the material.

Figure 6.1 shows the (103) Bragg reflection from the unstrained material before laser excitation, and 200 ps after laser excitation. The detector images have been rotated so that the scattering vector Q increases upwards along the vertical axis. The length of the scattering vector corresponds to a certain d-spacing, and by extension, a certain strain. Thus, a signal at a specific position on the detector indicates the presence of a strain wave. It can clearly be seen in Figure 6.1 that a number of atomic layers are strained after laser excitation. The intensity of

the signal is a measure of the number of layers experiencing a certain strain. The graphite sample can be assumed to be an imperfect crystal, in which case the intensity is proportional to the thickness of the diffracting material. A clear picture of the strain wave travelling through the material can thus be derived from the Bragg reflection. The experimental data were compared with simulations based on hydrodynamics. The 1D hydrodynamic code ESTHER[43] was used to simulate the evolution of mass density after laser illumination. Based on the results obtained from ESTHER simulations, a strain map depicting the evolution of strain over time in the probe depth was constructed by calculating the strain from the relation: $S(t) = \rho_0/\rho(t) - 1$, and is shown in Figure 6.2.

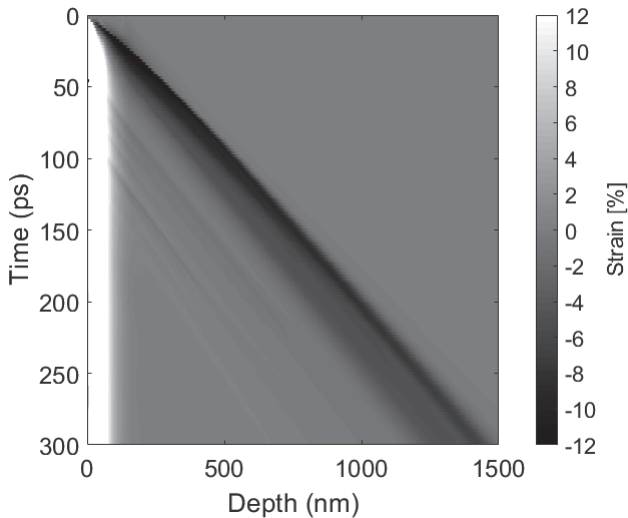


Figure 6.2: Map of the strain wave in time and depth. The strain wave increases in width and decreases in amplitude as it travels further into the sample. A constant positive strain can be observed at the surface.

The compressive strain wave can be seen to move into the sample, becoming broader and decreasing in amplitude as it travels. The simulated strain wave was used as input in an X-ray diffraction code to calculate the X-ray diffraction pattern. The experimental data were acquired using X-ray pulses with a duration of 100 ps, during which time the strain wave evolved. However, X-ray diffraction patterns calculated from the simulated wave correspond to one instance in time. For accurate comparison with the simulation, one diffraction pattern was constructed by adding together several diffraction patterns corresponding to different instances during the pulse duration, weighted according to the intensity of the X-ray pulse at the time. Figure 6.3 shows the simulated X-ray diffraction spot together with the experimental data.

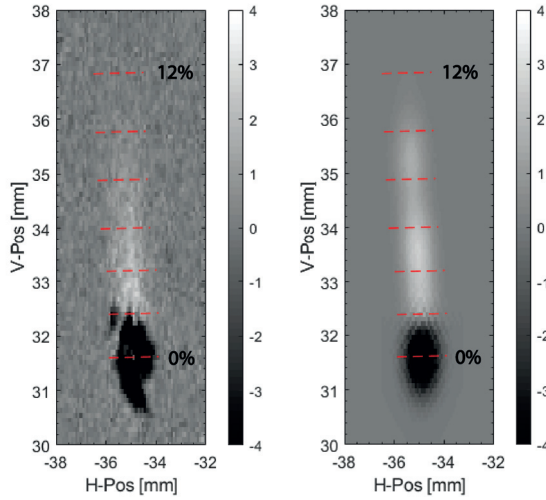


Figure 6.3: Difference images: Experimental data (left) and simulation (right). The vertical axis corresponds to the length of the scattering vector of the reflection. The white area indicates where the Bragg reflection has moved. The increase in the length of the scattering vector indicates compression of the crystallographic planes.

The pressure is obtained from the strain via the bulk modulus, and was calculated to be 7.2 GPa, 100 ps after laser excitation. After 200 ps, the pressure had decreased to 4.8 GPa. In order to draw any conclusions on the possibility of phase transitions, the temperature of the sample must also be determined. The temperature was obtained from the hydrodynamic simulation, and was determined to be below 315 K. Thus, the sample was in the diamond region of the phase diagram shown in Figure 6.4. However, it was not possible to confirm the formation of diamonds from the acquired X-ray diffraction patterns.

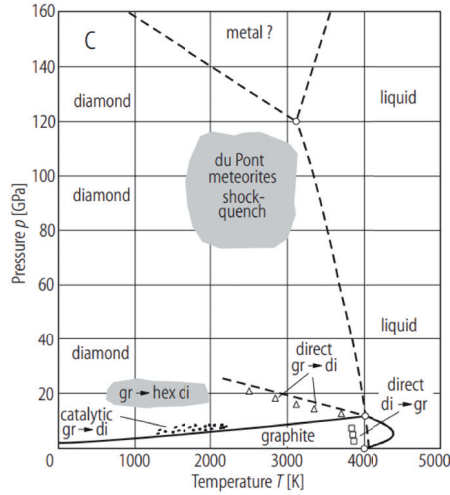


Figure 6.4: Carbon phase diagram showing the conditions under which the different phases are stable.[44]

6.2 Non-thermal melting in InSb

In a solid semiconductor, the electrons reside in the valence band, and the atoms are held together by covalent bonds. The electrons can be excited into anti-bonding conduction band orbitals using ultrashort laser pulses. If the excitation effect is sufficiently large, the potential landscape of the lattice will be significantly altered, and the atoms will no longer be held together, but instead break away forming a fluid state. For this to occur, approximately 10% of the electrons must be excited into the conduction band[16]. This is an ultrafast process that takes place on the sub-picosecond timescale, thus being distinguishable from thermal melting.

Non-thermal melting is a phenomenon mostly observed in semiconductors. The response to optically induced excitation of the electron system is quantitatively different in metals. The density of states in metals is largely unaffected by the increase in electron temperature[45]. Therefore, electronic excitation has a smaller impact on the lattice stability of free-electron metals. As a consequence, melting in metals is a purely thermal process[46]. It has, however, been reported that some non-thermal effects, such as bond hardening, may occur in noble metals such as gold[45].

The inertial model proposed by Lindenberg et al. in 2005 describes the process of non-thermal melting in semiconductors. In this model it is assumed that when

the covalent bonds between the atoms are broken by laser irradiation, the atoms will continue to move with their initial velocity due to their thermal energy. This model has been challenged by some theoreticians who claimed that the velocity of the atoms is the result of acceleration due to the modified potential surface of the system. In order to settle the controversy, measurements of the melting time can be performed at varying initial thermal energy of the atoms, which can be accomplished by heating and cooling the sample to different temperatures. If the inertial model is correct, the melting time will vary with the initial sample temperature. Such an experiment was performed at the FemtoMAX beamline in order to elucidate the process of non-thermal melting (Paper IV).

The sample used was an InSb wafer, cut with the (111) plane at an angle of 30° to the surface plane in order to enable a grazing angle of incidence in the experiment. The angle of incidence of the probe beam was set to 0.75° , so that the X-rays would only probe the molten part of the sample. The probe depth at this angle is 28 nm (1/e), i.e., much shorter than the 100 nm absorption depth of the laser.

The (111) reflection was probed with an X-ray beam of 3.56 keV, and the diffracted X-ray beam was captured with a CCD camera. The detector captures an image of the X-ray footprint on the sample. Non-thermal melting was induced with an 800 nm, femtosecond laser, delivering a fluence up to 150 mJ/cm^2 . The pump laser had an angle of incidence of 45° , allowing the spatial extension along the X-ray footprint to be mapped onto a time axis, as described in Section 3.4.5. The data were acquired in single-shot mode, as the effect is destructive, and a fresh sample position was used for each shot. Data were acquired from several shots in order to improve the signal-to-noise ratio. The measurements were performed at a number of temperatures between 35 K and 500 K.

The melting time, τ , was extracted for each shot by fitting a gaussian function to the temporal evolution of the X-ray intensity, in accordance with the Debye-Waller formalism:

$$I(t) = I_0 e^{-(t/\tau)^2} \quad (6.1)$$

The effect on the X-ray intensity after laser excitation over time is shown in Figure 6.5 for two different temperatures. The melting time is defined as the time taken for the signal to decrease from 90% to 10% of its initial value. It can clearly be seen from the different slopes that the melting time increases at lower sample temperatures.

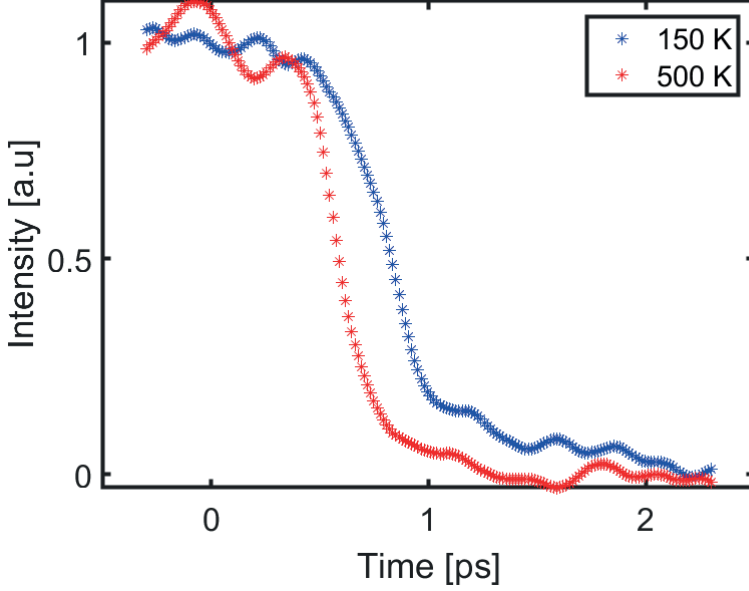


Figure 6.5: Temporal evolution of diffracted X-ray intensity.

The Debye-Waller formalism in Section 4.4.6 was used to perform theoretical calculations of the melting time as a function of temperature. The atomic velocities were calculated according to:

$$v_i = \sqrt{2U_{kin}/M} \quad (6.2)$$

where M is the average atomic mass and U_{kin} is equal to half the thermal vibrational energy, U , given by Equation 24.

$$U = 3k_B T \quad (6.3)$$

Figure 6.6 show the results together with the experimentally determined melting times. The red dashed line shows the prediction of the inertial model. In the temperature range 70 K to 500 K, this is a very good fit.

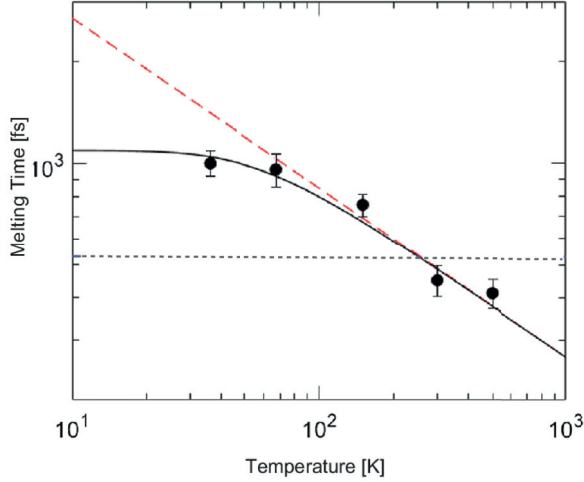


Figure 6.6: Melting time as a function of temperature. The black dashed curve is the melting time obtained when the inertial motion of the atoms is disregarded. The red dashed curve is the melting time obtained using the inertial model with the classical expression for the vibrational energy. The black curve is the inertial model when the zero-point energy is considered.

However, as the temperature approaches zero, the experimental melting time becomes constant. The classical expression for thermal vibrational energy in Equation 24 is inadequate to explain the behaviour of the system at very low temperatures. Instead, the zero-point energy should be used, which takes quantum fluctuations into account. This is included in Equation 25:

$$U = \frac{9}{8}k_B T_D + 3k_B T D_3\left(\frac{T_D}{T}\right) \quad (6.4)$$

where k_B is Boltzmann's constant, T_D is the Debye temperature, T is the temperature and $D_3(x)$ is the Debye function. The solid black curve in Figure 6.6 shows the melting time when quantum vibrational effects were taken into account when calculating the atomic velocity. This adjustment in the inertial model leads to an excellent fit to the data at all temperatures. It is thus clear from the experimental results that the initial velocity is an important factor during non-thermal melting, and that the inertial model can accurately describe the process of non-thermal melting.

6.3 Transition between thermal and non-thermal melting

The threshold for inducing non-thermal melting is higher than for thermal melting. Therefore, thermal melting will always be present during the melting process. In order to gain a complete picture of the melting process in semiconductors it is therefore necessary to understand the thermal melting process. In the thermal melting process, upon laser excitation, the laser energy is deposited in the electron system, which thereafter equilibrates with the lattice. It is well documented that the main channel for energy loss of the electron system is Fröhlich coupling to the longitudinal optical phonons. The optical phonons then decay into acoustic phonons, thus heating the lattice[47]. The coupling times of these processes govern the course of thermal melting. This has been studied in systems using low laser fluences[48]. There are however suggestions that the phonon coupling times are dependent on the excitation fluences[48, 49]. An experiment was conducted to study the thermal melting process in the transition regime between thermal and non-thermal melting, and is described in Paper VI. The experimental setup was the same as the one described in Section 6.2. The angle of incidence was 0.8° , corresponding to a probe depth of 35 nm at 3.6 keV. The laser fluence was varied between 30 and 70 mJ/cm². The temporal evolution of the melting process was captured by detecting the decrease in the diffracted intensity of the 111 Bragg peak. Figure 6.7 shows the temporal evolution of the diffracted X-ray intensity together with a theoretical model based on the time it takes to deposit energy larger than the latent heat of fusion at different depths in the sample.

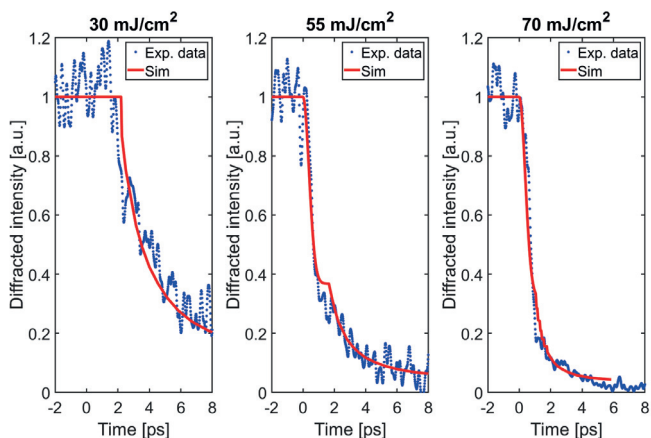


Figure 6.7: The diffracted X-ray intensity for 30 mJ/cm², 55 mJ/cm² and 70 mJ/cm².

The fast initial drop in the diffracted X-ray intensity that can be seen in the graphs for fluences of 50 mJ/cm² and 70 mJ/cm² is due to non-thermal melting. A slower drop, which is due to the thermal melting occurring at larger sample depths, is also visible after the initial drop. The non-thermal melting was modeled using a Gaussian function as described in Section 6.2. The threshold for non-thermal melting was determined to be 35 mJ/cm². In the data acquired at 30 mJ/cm² non-thermal melting is not observed, and the melting process is assumed to be purely thermal in this case. The thermal melting was modeled by solving the system of Equations 3.2. The initial condition was the energy deposited in the electron system. Non-linear absorption was used to calculate the fluence profile through the sample, using the first and second order of non-linear coefficients as described by Rousse et al.[15]. The best fit of the data was found for a second order coefficient of 235 cmGW⁻¹, which is lower than the value given by Rousse et al. However, the effective absorption depths in this study were determined to be 40 nm for 70mJ/cm², 45 nm for 55 mJ/cm² and 60 nm for 30 mJ/cm², which is in good agreement with studies performed by other groups[13, 50]. The phonon-phonon coupling time, τ_{oa} , determines how fast sufficient energy for melting is deposited in the lattice.

In the model presented here, only the first two coefficients of the non-linear absorption are taken into account. Electron diffusion was not taken into account. This would have an effect on the initial energy profile in the sample, with the electron distribution not following the optical distribution as assumed here. The melting time would still be governed by the coupling times between the electron and optical and acoustic phonon systems. Heat diffusion in the lattice was not taken into account, as it was determined through simulations that the timescale for diffusion is much too long, tens of picoseconds, to be relevant in this study.

The coupling times for the optical phonon - acoustic phonon interaction deduced from the data are shown in the table below:

Fluence [mJ/cm ²]	τ_{oa} [ps]
30	6
55	4
70	2

The coupling times for the higher fluences are significantly shorter than what has been reported for lower fluences, which is in line with what has been suggested.

Chapter 7

Controlling and Diagnosing the Temporal Properties of X-rays

The light-matter interactions described in this thesis are not only of fundamental interest, they can also be used in applications relevant at synchrotron radiation facilities. Laser-induced strain waves can be created to modulate the phonon spectrum, in order to create short X-ray pulses for applications in time-resolved experiments where a higher temporal resolution is needed than is typically available at storage ring facilities. Non-thermal melting can also be used as a timing device for pump/probe experiments.

7.1 An X-ray switch based on a photo-acoustic transducer

Experiments conducted at synchrotron radiation facilities are vital to the field of structural dynamics. However, the number of facilities providing X-ray pulses with short duration is limited, the typical pulse duration at a synchrotron radiation facility being 100 ps[51]. There are a number of schemes used at facilities to achieve short pulse durations, such as low-alpha mode [52] and femtoslicing[53], but these impact not only one beamline, but the whole facility. Being able to reduce the pulse duration at specific beamlines when needed would thus be advantageous. A photo-acoustic transducer can be used as an effective method

of reducing the pulse duration of a 100 ps X-ray pulse. This scheme can be implemented at beamlines without affecting the rest of the facility[54].

Coherent phonons provide additional means of fulfilling the scattering condition, and will introduce sidebands into the X-ray diffraction efficiency together with the Bragg peak[55, 56]. The photo-acoustic transducer is based on switching the X-ray diffraction efficiency of a crystal through modulation of the phonon spectrum. In this case, the transducer was composed of a thin gold film deposited on the surface of an InSb crystal. The gold film is heated by an optical laser pulse, and the expansion created launches a compressive strain wave from the Au/InSb interface through the sample. Two expansive strain waves are also generated at the vacuum/Au and Au/InSb interfaces, which counter-propagate through the film, launching a new strain wave through the InSb crystal for each reflection at the Au/InSb surface. The resulting strain wave through the InSb, will modulate the phonon spectrum, cancelling or enhancing phonons depending on their periods.

In this experiment, the sample consisted of a 60 nm thick gold film deposited on a (111) InSb crystal. The sample was pumped using a Ti:sapphire amplifier, delivering 60 fs laser pulses at 800 nm and 33 mJ/cm^2 . The response of the sample was probed with X-ray pulses with a 2 ps pulse duration at an energy offset of -8 eV from the (111) Bragg peak. The diffracted X-ray intensity was detected with a CCD camera for different time delays between the laser and X-ray beam in order to investigate the temporal evolution of the X-ray diffraction efficiency.

The optical absorption depth of gold at 800 nm is about 10 nm, meaning that all the energy from the laser pulse was absorbed by the metal film, and none in the InSb. The energy is first deposited in the electron system. Due to the fast electron motion and the weak electron-phonon interaction in gold, the pump energy will be distributed in the electron system throughout the whole of the gold film before the electron and the lattice systems become equilibrated. The lattice is heated within a few ps. Hot electrons in the gold film will travel into the sample, however, the interface between the gold film and the InSb crystal forms a barrier that the electrons cannot overcome, so there will be no electronic excitation of InSb.

The heat deposition in the sample can be modelled by the Two-Temperature Model described in Section 3.1. The `udkm1Dim` toolbox[57, 58], which implements the Two-Temperature Model, was used to simulate the strain wave and the X-ray diffraction efficiency. A map of the simulated X-ray diffraction efficiency is shown in Figure 7.1

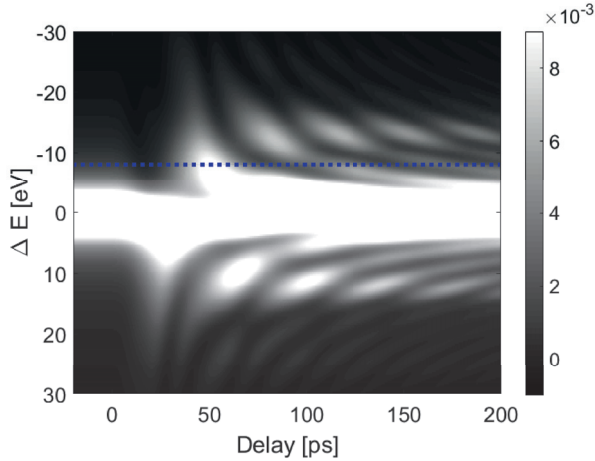


Figure 7.1: Simulated X-ray diffraction efficiency map. The blue dashed line indicates the first cancelled phonon mode.

The experimentally measured X-ray diffraction efficiency at an energy offset of -8.2 eV is shown in Figure 7.2 together with the results of the simulations, showing excellent agreement. The effect of the X-ray switch is a 20 ps long pulse with 8% of the power of the incidence beam.

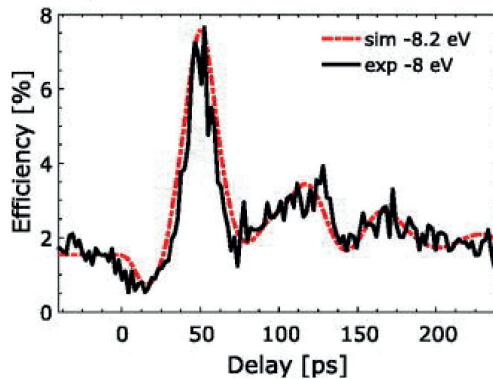


Figure 7.2: X-ray diffraction efficiency when probed -8 eV from the Bragg peak.

7.2 Non-thermal melting of InSb as a timing monitor

It is crucial in pump/probe experiments to know the precise timing between the pump and probe beams. All experiments involving a laser locked to an accelerator will suffer from temporal jitter, which will limit the temporal resolution

achievable. In order to evaluate the data from such experiments, the difference in time between the pump and probe beams must be accurately determined. A number of different methods can be used to measure this at synchrotron radiation facilities, for example, using a streak camera [59, 60] or devices based on electro-optical sampling [61].

It has been suggested that non-thermal melting can be used as a timing tool. The rapid decrease in X-ray reflectivity as the sample melts provides a clear time stamp, giving the relative time between the arrival of the pump and probe beams for each shot. Furthermore, it is relatively simple to implement at a beamline. For a scheme based on non-thermal melting to be practical, it must be possible to perform measurements at the same position on the sample many times. InSb resolidifies after melting, allowing multiple measurements at the same position. However, imperfections will form during crystal regrowth over time, which will lead to uncertainties in the timing measurement. It is therefore important to determine the optimal conditions for such measurements, to ensure that reliable results are obtained. In the experiment described in Paper V, the influence of sample temperature and laser fluence was evaluated. Such a non-thermal melting timing device can be used as a permanent timing device at a beamline, or to evaluate another timing device. During this experiment, non-thermal melting was used to evaluate a timing device being developed at the FemtoMAX beamline.

The experiment was performed at the FemtoMAX beamline at MAX IV. The sample was an InSb wafer cut with the [111] plane at 30° to the surface. Non-thermal melting was induced by an 800 nm fs laser, and probed by X-rays in a grazing geometry. The method of choosing the incidence angle was described in Section 4.4. The difference in the angle of incidence between the laser and X-ray beams allowed the temporal evolution of the melting process to be captured using the space-time mapping method described in Section 4.4. The measurements were performed at temperatures ranging from room temperature to 500 K, in order to determine the optimal conditions. Data were obtained from a large number of laser/X-ray shots acquired from the same position on the sample, and analysed to determine how such a timing device would function over time. For every laser/X-ray shot, a reference shot using only the X-ray beam was performed in order to investigate how the diffracted X-ray signal was affected by cumulative laser damage.

In order to deduce the pump/probe timing from the diffracted X-ray signal, a gaussian function was fitted to an outline in the temporal direction of the data. Time zero was defined as the time at which the X-ray signal had decreased to 50%. (This is shown in Figure 7.3)

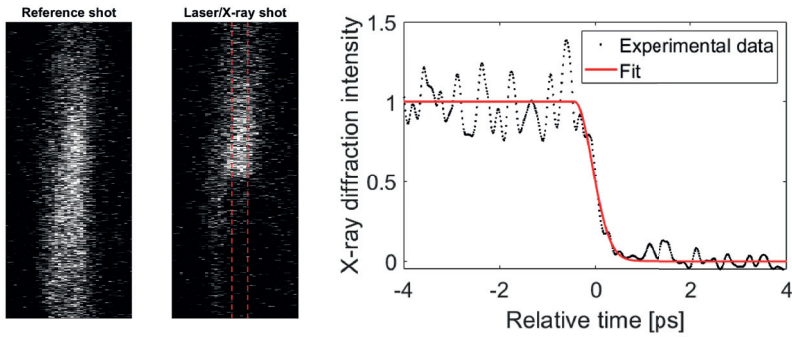


Figure 7.3: The reference shot using only the X-ray beam a), and the shot with the laser beam b). Time increases from the top of the images to the bottom. The area indicated by the red dashed lines in the laser shot indicates the part of the image used in the analysis, where the laser has a uniform fluence. c) The laser shot (normalised using the reference shot) together with a gaussian fit. Time zero is defined as the time at which the intensity had decreased to $\approx 50\%$. This dataset was acquired at 300 K

Figure 7.4 shows the diffracted X-ray beam in the reference shots before the first and the 10th shots for measurements at 300 K and 500 K. A significant difference can be seen between these two temperatures. At room temperature, the sample is destroyed after a few shots, and it quickly becomes impossible to accurately extract time zero due to the low X-ray signal.

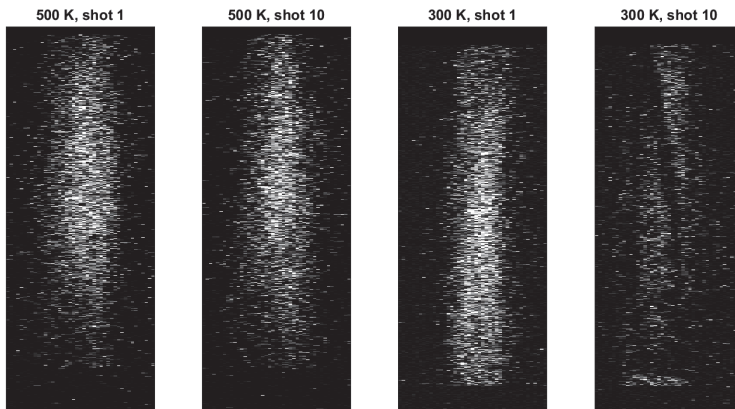


Figure 7.4: The diffracted X-ray signal before the 1st and 10th laser shots at 300 K and 500 K.

The effect of sample temperature on the X-ray diffraction efficiency can be quantified by investigating the change in the integrated signal in the reference shots after each laser shot. The results are shown in Figure 7.5. At room temperature, the intensity of the diffracted X-ray beam is drastically decreased

after only a few shots. However, at higher sample temperatures, the X-ray intensity is still 50% of the initial after up to 200 shots, suggesting that the regrowth of InSb is facilitated at higher temperatures.

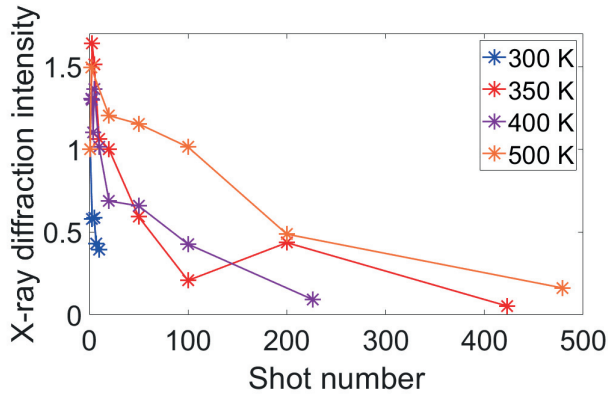


Figure 7.5: The diffraction X-ray intensity of reference shots as a function of the number of shots at the different temperatures investigated. The intensity is normalised to the intensity of the first shot at each temperature.

Figure 7.6 shows the diffracted X-ray intensity after 20 shots at 500 K, where it can be seen that the diffracted X-ray intensity increases after time zero [after a few shots], indicated by the green box. This is due to laser-induced periodic surface structures, as described in Section 3.3.

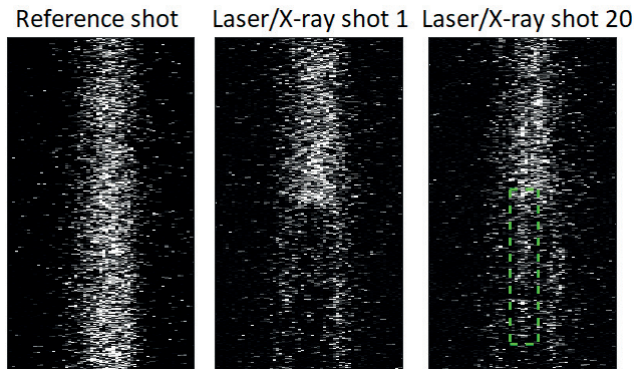


Figure 7.6: Images of (a) the reference shot, (b) the 1st laser/X-ray shot on the pristine sample and (c) the 20th laser/X-ray shot at the same position. The green dashed rectangle indicates the increase in X-ray diffraction intensity seen in the later shots. The data were acquired at 500 K

Figure 7.7 shows microscope images of the sample after 10 shots and 200 shots.

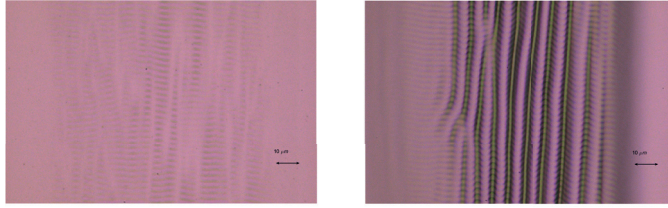


Figure 7.7: Microscope images of the surface of the sample after laser exposure to 10 shots (left) and 200 shots (right). The sample temperature during data acquisition was 500 K

The effect of laser-induced periodic structures on timing was evaluated by measuring the edge contrast in the temporal trace. The edge contrast is defined as $(I_0 - I_{1ps})/I_0$, where I_0 is the intensity before laser excitation, and I_{1ps} is the intensity 1 ps after laser excitation. The edge contrast was determined for two different fluences, and the results are presented in Figure 7.8. The laser footprint will show some variation in fluence in the horizontal direction. The X-ray diffraction signal was divided into a centre section and a section consisting of the sides, corresponding to sample positions that have been excited by higher and lower fluences, and the edge contrast was evaluated separately. The fluence in the centre was 130 mJ/cm^2 and that in the sides 90 mJ/cm^2 . These values are sufficient to induce non-thermal melting, but are not in the regime where Hillyard et al. found accelerated disordering[62]. The edge contrast was reduced in both regions during the first 20 shots, but remained fairly constant between 20 and 200 shots. The edge contrast was slightly better in the data from the edges where the fluence was lower.

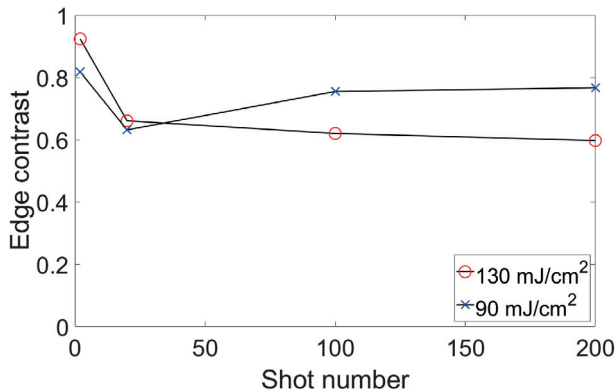


Figure 7.8: Edge contrast after 20, 100 and 200 shots in the central region (o) with higher fluence (130 mJ/cm^2), and the sides (x) where the fluence was lower (90 mJ/cm^2).

The accuracy of the timing monitor was evaluated by dividing the detector image into two halves, and evaluating the right and left halves of the X-ray diffraction spot separately, treating them as though they had been acquired using two identical set-ups.

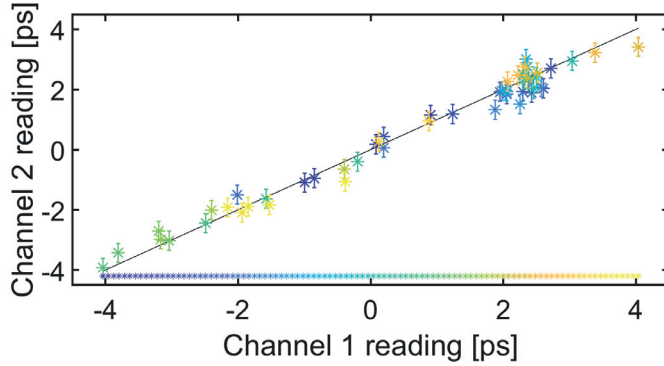


Figure 7.9: The graph shows the correlation between the two sets of data, from the right and left halves of the diffraction spot. The data points are plotted on a colour scale ranging from purple to yellow, where purple is the first shot and yellow the last shot.

The correlation between the two sets of data provides a measure of the accuracy of the timing monitor, and is shown in Figure 7.9. The accuracy deduced from the square root of the standard deviation was 230 fs.

Chapter 8

Summary and Outlook

8.1 Summary

A large-amplitude strain wave was generated in graphite by melting the sample surface, and the pressure related to the strain wave was determined to be 7.2 GPa (Paper III). At room temperature, this is in the region in the phase diagram where the diamond phase is stable, suggesting that a strain wave generated by an ultrashort laser pulse could drive the graphite-to-diamond phase transition.

The non-thermal melting time in InSb was determined over a wide range of sample temperatures in order to evaluate the inertial model, and the disordering time was found to be dependent on the sample temperature. It was discovered that when the zero-point vibrational energy was taken into account, the inertial model predicted the atomic motion during the process of non-thermal melting well (Paper IV).

The effect of a photo-acoustic transducer on an X-ray pulse was studied. Laser excitation of a thin gold film was used to generate a strain wave in an InSb crystal, allowing the phonon spectrum to be modulated (Paper I). The X-ray switch was used to modulate the X-ray reflectivity converting a 100 ps X-ray pulse into a 20 ps pulse with an efficiency of 8%.

The possibility of using non-thermal melting of InSb as a timing device was evaluated. The effects of laser fluence and sample temperature were investigated in order to determine the optimal conditions. It was established that when heated above room temperature, the sample could be irradiated at the same position up to 200 times (Paper V). The experimental set-up was also used to

evaluate a timing device being developed at the FemtoMAX beamline.

The transition between thermal and non-thermal melting was studied in InSb (Paper VI). It was shown that thermal melting can explain the exponential tail in the temporal evolution of the intensity of the Bragg peak. Phonon-phonon coupling times for high fluences were deduced from the attenuation of the diffracted X-ray signal.

8.2 Outlook

Time-resolved X-ray diffraction experiments can be used to elucidate fast processes in materials on the atomic scale, and there is a wealth of applications that require careful determination of such material properties. 2D materials are very useful in technological applications, and it is thus important to be able to determine their properties accurately. 2D materials such as graphene and black phosphorus are highly anisotropic. The cross-plane heat conductivity varies with the sample thickness for thin samples, and can be difficult to measure, so there is considerable interest in developing reliable methods to study this. Thin samples of black phosphorus have been produced by our group, and measurements have been performed using time-resolved X-ray diffraction, which are currently being analysed. Efforts are also being made to set up electron diffraction experiments using thin black phosphorus samples.

A THz generation set-up based on optical rectification in organic crystals was recently implemented at the FemtoMAX beamline. THz radiation can be used to excite certain phonon modes in InSb. Excitation of these phonon modes could have a considerable impact on the nearly forbidden reflections, as discussed in Section 4.1.6. Measurements have recently been made and the data are being analysed.

Based on the findings presented in Paper V, it was concluded that increasing the sample temperature enabled regrowth of the InSb crystal. However, it was not possible to determine the exact process of regrowth. Further measurements should be performed to elucidate the physics governing the regrowth process.

References

- [1] K. S. Novoselov, A. K. Geim, S. V. Morozov, D. Jiang, Y. Zhang, S. V. Dubonos, I. V. Grigorieva, and A. A. Firsov. Electric field effect in atomically thin carbon films. *Science*, 306(5696):666–669, 2004. 866en Times Cited:44945 Cited References Count:16.
- [2] A. A. Balandin. Thermal properties of graphene and nanostructured carbon materials. *Nature Materials*, 10(8):569–581, 2011. 795ty Times Cited:3946 Cited References Count:148.
- [3] J. Y. Luo, X. Zhao, J. S. Wu, H. D. Jang, H. H. Kung, and J. X. Huang. Crumpled graphene-encapsulated si nanoparticles for lithium ion battery anodes. *Journal of Physical Chemistry Letters*, 3(13):1824–1829, 2012. 972bq Times Cited:415 Cited References Count:39.
- [4] I. Kimukin, N. Biyikli, T. Kartaloglu, O. Aytur, and E. Ozbay. High-speed insb photodetectors on gaas for mid-ir applications. *Ieee Journal of Selected Topics in Quantum Electronics*, 10(4):766–770, 2004. 862kg Times Cited:42 Cited References Count:17.
- [5] H. Z. Chen, X. H. Sun, K. W. C. Lai, M. Meyyappan, and N. Xi. Infrared detection using an insb nanowire. *2009 Ieee Nanotechnology Materials and Devices Conference*, pages 212–+, 2009. Bmu53 Times Cited:27 Cited References Count:17 IEEE Nanotechnology Materials and Devices Conference.
- [6] K. F. Hulme and J. B. Mullin. Indium antimonide - a review of its preparation, properties and device applications. *Solid-State Electronics*, 5(Jul-A):211–+, 1962. Xl023 Times Cited:130 Cited References Count:204.
- [7] W. H. Bragg and W. L. Bragg. The reflection of x-rays by crystals. *Proceedings of the Royal Society of London Series a-Containing Papers of a Mathematical and Physical Character*, 88(605):428–438, 1913. V41jv Times Cited:653 Cited References Count:2.

- [8] B. Rethfeld, K. Sokolowski-Tinten, D. von der Linde, and S. I. Anisimov. Timescales in the response of materials to femtosecond laser excitation. *Applied Physics a-Materials Science Processing*, 79(4-6):767–769, 2004. 839el Times Cited:225 Cited References Count:19.
- [9] A. I. H. Persson, A. Jarnac, X. C. Wang, H. Enquist, A. Jurgilaitis, and J. Larsson. Studies of electron diffusion in photo-excited ni using time-resolved x-ray diffraction. *Applied Physics Letters*, 109(20), 2016. Ec3br Times Cited:2 Cited References Count:29.
- [10] M. Harb, H. Enquist, A. Jurgilaitis, F. T. Tuyakova, A. N. Obraztsov, and J. Larsson. Phonon-phonon interactions in photoexcited graphite studied by ultrafast electron diffraction. *Physical Review B*, 93(10), 2016. Dg0df Times Cited:23 Cited References Count:28.
- [11] J. A. Vanvechten, R. Tsu, F. W. Saris, and D. Hoonhout. Reasons to believe pulsed laser annealing of si does not involve simple thermal melting. *Physics Letters A*, 74(6):417–421, 1979. Hz083 Times Cited:137 Cited References Count:34.
- [12] I. L. Shumay and U. Hofer. Phase transformations of an insb surface induced by strong femtosecond laser pulses. *Physical Review B*, 53(23):15878–15884, 1996. Ut770 Times Cited:85 Cited References Count:31.
- [13] K. J. Gaffney, A. M. Lindenberg, J. Larsson, K. Sokolowski-Tinten, C. Blome, O. Synnergren, J. Sheppard, C. Caleman, A. G. MacPhee, D. Weinstein, D. P. Lowney, T. Allison, T. Matthews, R. W. Falcone, A. L. Cavalieri, D. M. Fritz, S. H. Lee, P. H. Bucksbaum, D. A. Reis, J. Rudati, A. T. Macrander, P. H. Fuoss, C. C. Kao, D. P. Siddons, R. Pahl, K. Moffat, J. Als-Nielsen, S. Duesterer, R. Ischebeck, H. Scharb, H. Schulte-Schrepping, J. Schneider, D. von der Linde, O. Hignette, F. Sette, H. N. Chapman, R. W. Lee, T. N. Hansen, J. S. Wark, M. Bergh, G. Huldt, D. van der Spoel, N. Timneanu, J. Hajdu, R. A. Akre, E. Bong, P. Krejcik, J. Arthur, S. Brennan, K. Luening, and J. B. Hastings. Observation of structural anisotropy and the onset of liquidlike motion during the nonthermal melting of insb. *Phys Rev Lett*, 95(12):125701, 2005.
- [14] E. Zijlstra, J. Walkenhorst, C. Gilfert, C. Sippel, W. Tows, and M. Garcia. Ab initio description of the first stages of laser-induced ultra-fast nonthermal melting of insb. *Applied Physics B-Lasers and Optics*, 93(4):743–747, 2008. 374er Times Cited:11 Cited References Count:14.
- [15] A. Rousse, C. Rischel, S. Fourmaux, I. Uschmann, S. Sebban, G. Grillon, P. Balcou, E. Foster, J. P. Geindre, P. Audebert, J. C. Gauthier, and

- D. Hulin. Non-thermal melting in semiconductors measured at femtosecond resolution. *Nature*, 410(6824):65–68, 2001. 406bd Times Cited:560 Cited References Count:28.
- [16] K. H. Bennemann. Ultrafast dynamics in solids. *Journal of Physics-Condensed Matter*, 16(30):R995–R1056, 2004. 847xl Times Cited:44 Cited References Count:103.
- [17] P. Stampfli and K. H. Bennemann. Time-dependence of the laser-induced femtosecond lattice instability of si and gaas - role of longitudinal optical distortions. *Physical Review B*, 49(11):7299–7305, 1994. Nc463 Times Cited:216 Cited References Count:29.
- [18] A. M. Lindenberg. Atomic-scale visualization of inertial dynamics (vol 308, pg 392, 2005). *Science*, 308(5730):1870–1870, 2005. 940bz Times Cited:0 Cited References Count:2.
- [19] E. S. Zijlstra, J. Walkenhorst, and M. E. Garcia. Anharmonic noninertial lattice dynamics during ultrafast nonthermal melting of insb. *Physical Review Letters*, 101(13), 2008. 355ai Times Cited:51 Cited References Count:23.
- [20] M. Birnbaum. Semiconductor surface damage produced by ruby lasers. *Journal of Applied Physics*, 36(11):3688–, 1965. 70363 Times Cited:680 Cited References Count:6.
- [21] A. Jurgilaitis, R. Nuske, H. Enquist, H. Navirian, P. Sondhauss, and J. Larsson. X-ray diffraction from the ripple structures created by femtosecond laser pulses. *Applied Physics a-Materials Science Processing*, 100(1):105–112, 2010. 615ih Times Cited:2 Cited References Count:30.
- [22] X. C. Wang, G. C. Lim, F. L. Ng, W. Liu, and S. J. Chua. Femtosecond pulsed laser-induced periodic surface structures on gan/sapphire. *Applied Surface Science*, 252(5):1492–1497, 2005. 993wh Times Cited:32 Cited References Count:19.
- [23] C. Thomsen, H. T. Grahn, H. J. Maris, and J. Tauc. Surface generation and detection of phonons by picosecond light pulses. *Phys. Rev. B*, 34:4129–4138, Sep 1986.
- [24] C. Thomsen, J. Strait, Z. Vardeny, H. J. Maris, J. Tauc, and J. J. Hauser. Coherent phonon generation and detection by picosecond light-pulses. *Physical Review Letters*, 53(10):989–992, 1984. Tf797 Times Cited:382 Cited References Count:11.

- [25] T. Smausz, B. Kondasz, T. Gera, T. Ajtai, N. Utry, M. Pinter, G. Kiss-Albert, J. Budai, Z. Bozoki, G. Szabo, and B. Hopp. Determination of uv-visible-nir absorption coefficient of graphite bulk using direct and indirect methods. *Applied Physics a-Materials Science Processing*, 123(10), 2017. Fj5ft Times Cited:13 Cited References Count:22.
- [26] *Handbook of the Physicochemical Properties of the Elements*. Plenum Publishing Corporation, New York, 1968.
- [27] O. Synnergren, T. N. Hansen, S. Canton, H. Enquist, P. Sondhauss, A. Srivastava, and J. Larsson. Coherent phonon control. *Applied Physics Letters*, 90(17), 2007. 169bv Times Cited:7 Cited References Count:31.
- [28] P. Gaal, D. Schick, M. Herzog, A. Bojahr, R. Shayduk, J. Goldshteyn, W. Leitenberger, I. Vrejoiu, D. Khakhulin, M. Wulff, and M. Bargheer. Ultrafast switching of hard x-rays. *Journal of Synchrotron Radiation*, 21:380–385, 2014. 2 Ab5oa Times Cited:9 Cited References Count:30.
- [29] B. E. Warren. *X-ray diffraction*. Addison-Wesley series in metallurgy and materials. Addison-Wesley Pub. Co., Reading, Mass., 1969. 68025928 (Bertram Eugene), [by] B. E. Warren. illus. 24 cm.
- [30] B. L. Henke, E. M. Gullikson, and J. C. Davis. X-ray interactions - photoabsorption, scattering, transmission and reflection at $e=50\text{--}30,000$ ev, $z=1\text{--}92$ (vol 54, pg 181, 1993). *Atomic Data and Nuclear Data Tables*, 55(2):349–349, 1993. Mr225 Times Cited:39 Cited References Count:1.
- [31] J. Weisshaupt, V. Juve, M. Holtz, S. A. Ku, M. Woerner, T. Elsaesser, S. Alisuskas, A. Pugzlys, and A. Baltuska. High-brightness table-top hard x-ray source driven by sub-100-femtosecond mid-infrared pulses. *Nature Photonics*, 8(12):927–930, 2014. Au8ag Times Cited:122 Cited References Count:22.
- [32] G. Korn, A. Thoss, H. Stiel, U. Vogt, M. Richardson, T. Elsaesser, and M. Faubel. Ultrashort 1-khz laser plasma hard x-ray source. *Optics Letters*, 27(10):866–868, 2002. 555gj Times Cited:82 Cited References Count:21.
- [33] P. Emma, R. Akre, J. Arthur, R. Bionta, C. Bostedt, J. Bozek, A. Brachmann, P. Bucksbaum, R. Coffee, F. J. Decker, Y. Ding, D. Dowell, S. Edstrom, A. Fisher, J. Frisch, S. Gilevich, J. Hastings, G. Hays, P. Hering, Z. Huang, R. Iverson, H. Loos, M. Messerschmidt, A. Miahnahri, S. Moeller, H. D. Nuhn, G. Pile, D. Ratner, J. Rzepiela, D. Schultz, T. Smith, P. Stefan, H. Tompkins, J. Turner, J. Welch, W. White, J. Wu,

- G. Yocky, and J. Galayda. First lasing and operation of an angstrom-wavelength free-electron laser. *Nature Photonics*, 4(9):641–647, 2010. 645no Times Cited:2129 Cited References Count:43.
- [34] T. Tschentscher, C. Bressler, J. Grunert, A. Madsen, A. P. Mancuso, M. Meyer, A. Scherz, H. Sinn, and U. Zastra. Photon beam transport and scientific instruments at the european xfel. *Applied Sciences-Basel*, 7(6), 2017. Ez1do Times Cited:140 Cited References Count:125.
- [35] J. R. Schneider E. J. Jaeschke, S. Khan and J. B. Hastings. *Synchrotron Light Sources and Free-electron Lasers: Accelerator Physics, Instrumentation and Science Applications*. Springer.
- [36] *Synchrotron Physics*, pages 39–86. 2011.
- [37] S. Werin. *Accelerator technique*. Max-lab, 2.5 edition, 2006.
- [38] A. Hirsch. The era of carbon allotropes. *Nature Materials*, 9(11):868–871, 2010. 669ma Times Cited:650 Cited References Count:23.
- [39] G. W. Yang and J. B. Wang. Pulsed-laser-induced transformation path of graphite to diamond via an intermediate rhombohedral graphite. *Applied Physics a-Materials Science Processing*, 72(4):475–479, 2001. 417nc Times Cited:62 Cited References Count:25.
- [40] R. Nuske, A. Jurgilaitis, H. Enquist, M. Harb, Y. Fang, U. Hakanson, and J. Larsson. Transforming graphite to nanoscale diamonds by a femtosecond laser pulse. *Applied Physics Letters*, 100(4), 2012. 889ho Times Cited:21 Cited References Count:29.
- [41] G. W. Yang, J. B. Wang, and Q. X. Liu. Preparation of nano-crystalline diamonds using pulsed laser induced reactive quenching. *Journal of Physics-Condensed Matter*, 10(35):7923–7927, 1998. 119qb Times Cited:199 Cited References Count:22.
- [42] C. J. Mundy, A. Curioni, N. Goldman, I. F. W. Kuo, E. J. Reed, L. E. Fried, and M. Ianuzzi. Ultrafast transformation of graphite to diamond: An ab initio study of graphite under shock compression. *Journal of Chemical Physics*, 128(18), 2008. 302qj Times Cited:77 Cited References Count:34.
- [43] J. P. Colombier, P. Combis, F. Bonneau, R. Le Harzic, and E. Audouard. Hydrodynamic simulations of metal ablation by femtosecond laser irradiation. *Physical Review B*, 71(16), 2005. 921kl Times Cited:181 Cited References Count:37.

- [44] Diamond (c) phase diagram, equation of state: Datasheet from landolt-börnstein - group iii condensed matter · volume 41a1α: "group iv elements, iv-iv and iii-v compounds. part a - lattice properties" in springermaterials (https://doi.org/10.1007/10551045_168).
- [45] V. Recoules, J. Clerouin, G. Zerah, P. M. Anglade, and S. Mazevet. Effect of intense laser irradiation on the lattice stability of semiconductors and metals. *Physical Review Letters*, 96(5), 2006. 011fa Times Cited:205 Cited References Count:27.
- [46] M. Z. Mo, Z. Chen, R. K. Li, M. Dunning, B. B. L. Witte, J. K. Baldwin, L. B. Fletcher, J. B. Kim, A. Ng, R. Redmer, A. H. Reid, P. Shekhar, X. Z. Shen, M. Shen, K. Sokolowski-Tinten, Y. Y. Tsui, Y. Q. Wang, Q. Zheng, X. J. Wang, and S. H. Glenzer. Heterogeneous to homogeneous melting transition visualized with ultrafast electron diffraction. *Science*, 360(6396):1451–1454, 2018. Gk9tl Times Cited:60 Cited References Count:35.
- [47] A. H. Chin, R. W. Schoenlein, T. E. Glover, P. Balling, W. P. Leemans, and C. V. Shank. Ultrafast structural dynamics in insb probed by time-resolved x-ray diffraction. *Physical Review Letters*, 83(2):336–339, 1999. 215ac Times Cited:167 Cited References Count:23.
- [48] F. S. Krasniqi, S. L. Johnson, P. Beaud, M. Kaiser, D. Grolimund, and G. Ingold. Influence of lattice heating time on femtosecond laser-induced strain waves in insb. *Physical Review B*, 78(17), 2008. 376wu Times Cited:18 Cited References Count:49.
- [49] K. T. Tsen, J. G. Kiang, D. K. Ferry, and H. Morkoc. Subpicosecond time-resolved raman studies of field-induced transient transport in an inxgal-xas-based p-i-n semiconductor nanostructure. *Applied Physics Letters*, 89(26), 2006. 121kx Times Cited:4 Cited References Count:25.
- [50] P. B. Hillyard, K. J. Gaffney, A. M. Lindenberg, S. Engemann, R. A. Akre, J. Arthur, C. Blome, P. H. Bucksbaum, A. L. Cavalieri, A. Deb, R. W. Falcone, D. M. Fritz, P. H. Fuoss, J. Hajdu, P. Krejčík, J. Larsson, S. H. Lee, D. A. Meyer, A. J. Nelson, R. Pahl, D. A. Reis, J. Rudati, D. P. Siddons, K. Sokolowski-Tinten, D. von der Linde, and J. B. Hastings. Carrier-density-dependent lattice stability in insb (vol 98, pg 125501, 2007). *Physical Review Letters*, 98(14), 2007. 154mq Times Cited:2 Cited References Count:1.
- [51] P. H. Bucksbaum and R. Merlin. The phonon bragg switch: a proposal to generate sub-picosecond x-ray pulses. *Solid State Communications*, 111(10):535–539, 1999. 224ql Times Cited:56 Cited References Count:19.

- [52] I. P. S. Martin, G. Rehm, C. Thomas, and R. Bartolini. Experience with low-alpha lattices at the diamond light source. *Physical Review Special Topics-Accelerators and Beams*, 14(4), 2011. 750ea Times Cited:25 Cited References Count:36.
- [53] A. A. Zholents and M. S. Zolotarev. Femtosecond x-ray pulses of synchrotron radiation. *Physical Review Letters*, 76(6):912–915, 1996. Tt491 Times Cited:186 Cited References Count:9.
- [54] A. I. H. Persson, H. Enquist, A. Jurgilaitis, B. P. Andreasson, and J. Larsson. Real-time observation of coherent acoustic phonons generated by an acoustically mismatched optoacoustic transducer using x-ray diffraction. *Journal of Applied Physics*, 118(18), 2015. Cw5nf Times Cited:4 Cited References Count:35.
- [55] J. Larsson, A. Allen, P. H. Bucksbaum, R. W. Falcone, A. Lindenberg, G. Naylor, T. Missalla, D. A. Reis, K. Scheidt, A. Sjogren, P. Sondhauss, M. Wulff, and J. S. Wark. Picosecond x-ray diffraction studies of laser-excited acoustic phonons in insb. *Applied Physics a-Materials Science Processing*, 75(4):467–478, 2002. 572hl Times Cited:56 Cited References Count:15.
- [56] A. M. Lindenberg, I. Kang, S. L. Johnson, T. Missalla, P. A. Heimann, Z. Chang, J. Larsson, P. H. Bucksbaum, H. C. Kapteyn, H. A. Padmore, R. W. Lee, J. S. Wark, and R. W. Falcone. Time-resolved x-ray diffraction from coherent phonons during a laser-induced phase transition. *Physical Review Letters*, 84(1):111–114, 2000. 271hj Times Cited:314 Cited References Count:22.
- [57] D. Schick. udkm1dsim.
- [58] D. Schick, A. Bojahr, M. Herzog, R. Shayduk, C. V. Schmising, and M. Bargheer. Udkm1dsim—a simulation toolkit for 1d ultrafast dynamics in condensed matter. *Computer Physics Communications*, 185(2):651–660, 2014. 287jg Times Cited:37 Cited References Count:17.
- [59] G. A. Naylor, K. Scheidt, J. Larsson, M. Wulff, and J. M. Filhol. A sub-picosecond accumulating streak camera for x-rays. *Measurement Science and Technology*, 12(11):1858–1864, 2001. 498qw Times Cited:33 Cited References Count:22.
- [60] H. Enquist, H. Navirian, R. Nuske, C. V. Schmising, A. Jurgilaitis, M. Herzog, M. Bargheer, P. Sondhauss, and J. Larsson. Subpicosecond hard x-ray streak camera using single-photon counting. *Optics Letters*, 35(19):3219–3221, 2010. 656xq Times Cited:10 Cited References Count:17.

- [61] A. L. Cavalieri, D. M. Fritz, S. H. Lee, P. H. Bucksbaum, D. A. Reis, J. Rudati, D. M. Mills, P. H. Fuoss, G. B. Stephenson, C. C. Kao, D. P. Siddons, D. P. Lowney, A. G. MacPhee, D. Weinstein, R. W. Falcone, R. Pahl, J. Als-Nielsen, C. Blome, S. Dusterer, R. Ischebeck, H. Schlarb, H. Schulte-Schrepping, T. Tschentscher, J. Schneider, O. Hignette, F. Sette, K. Sokolowski-Tinten, H. N. Chapman, R. W. Lee, T. N. Hansen, O. Synnergren, J. Larsson, S. Techert, J. Sheppard, J. S. Wark, M. Bergh, C. Caleman, G. Hultdt, D. van der Spoel, N. Timneanu, J. Hajdu, R. A. Akre, E. Bong, P. Emma, P. Krejcik, J. Arthur, S. Brennan, K. J. Gaffney, A. M. Lindenberg, K. Luening, and J. B. Hastings. Clocking femtosecond x rays. *Physical Review Letters*, 94(11), 2005. 910ia Times Cited:204 Cited References Count:19.
- [62] K. J. Gaffney, P. B. Hillyard, A. M. Lindenberg, S. Engemann, A. Deb, and D. A. Meyer. Carrier dependent stability of a semiconductor lattice measured with femtosecond x-ray diffraction. *Ultrafast Phenomena Xv*, 88:710–+, 2007. Bgr37 Times Cited:0 Cited References Count:8 Springer Series in Chemical Physics.

Part II

Papers

Author's contributions

Paper I: Communication: Demonstration of a 20 ps X-ray switch based on a photoacoustic transducer

I participated in the running of the experiment, and took part in the data analysis. I gave feedback on the manuscript.

Paper II: FemtoMAX - an X-ray beamline for structural dynamics at the short-pulse facility of MAX IV

I participated in the experiments during the commissioning of the beamline and I gave feedback on the manuscript.

Paper III: Generation of a large compressive strain wave in graphite by ultrashort-pulse laser irradiation

I participated in the on-site data analysis during the experiment. I gave feedback on the manuscript.

Paper IV: Role of thermal equilibrium dynamics in atomic motion during nonthermal laser-induced melting

I participated in the planning and set-up of the experiment. I also participated in the data acquisition and analysis. I provided some of the figures for the paper, and gave feedback on the manuscript.

Paper V: Repetitive non-thermal melting as a timing monitor for femtosecond pump/probe X-ray experiments

I was responsible for the experiment. I performed data analysis both on-site and after the experiment. I wrote the draft of the manuscript and produced the figures.

Paper VI: The transition between thermal and non-thermal melting in InSb

I participated in planning the experiment and data acquisition. I analysed the data, implemented the model and wrote the first draft of the manuscript.



LUND UNIVERSITY
Faculty of Engineering, LTH
Department of Physics
Division of Atomic Physics

ISBN 978-91-8039-184-9
ISSN 0281-2762

Lund Reports on Atomic Physics, LRAP 579 (2022)

